



The Green Bank Ammonia Survey: Data Release 2

Downloaded from: <https://research.chalmers.se>, 2026-05-15 07:08 UTC

Citation for the original published paper (version of record):

Pineda, J., Friesen, R., Rosolowsky, E. et al (2026). The Green Bank Ammonia Survey: Data Release 2. *Astrophysical Journal, Supplement Series*, 282(1). <http://dx.doi.org/10.3847/1538-4365/ae11b1>

N.B. When citing this work, cite the original published paper.



The Green Bank Ammonia Survey: Data Release 2

Jaime E. Pineda¹ , and Rachel K. Friesen²

(co-PIs)

Erik Rosolowsky³ , Ana Chacón-Tanarro⁴ , Michael Chun-Yuan Chen⁵ , James Di Francesco^{6,7} , Helen Kirk^{6,7} , Anna Punanova⁸ , Youngmin Seo⁹ , Yancy Shirley¹⁰ , Adam Ginsburg¹¹ , Stella S. R. Offner¹² , Ayush Pandhi² , Ayushi Singh¹³ , Feiyu Quan¹⁴ , Héctor G. Arce¹⁵ , Paola Caselli¹ , Spandan Choudhury^{1,16} , Alyssa A. Goodman¹⁷ , Fabian Heitsch¹⁸ , Peter G. Martin¹⁹ , Christopher D. Matzner² , Philip C. Myers¹⁷ , Elena Redaelli^{1,20} , and Samantha Scibelli^{21,22}

(The GAS collaboration)

¹ Max Planck Institute for Extraterrestrial Physics, Gießenbachstraße 1, D-85748 Garching bei München, Germany; jpineda@mpe.mpg.de² Department of Astronomy & Astrophysics, University of Toronto, 50 Saint George Street, Toronto, ON, M5S 3H4, Canada³ Department of Physics, University of Alberta, Edmonton, AB, Canada⁴ Observatorio Astronómico Nacional (OAN-IGN), Alfonso XII 3, E-28014 Madrid, Spain⁵ Department for Physics, Engineering Physics and Astrophysics, Queen's University, Kingston, ON, K7L 3N6, Canada⁶ Department of Physics and Astronomy, University of Victoria, 3800 Finnerty Road, Victoria, BC, V8P 5C2, Canada⁷ Herzberg Astronomy and Astrophysics, National Research Council of Canada, 5071 West Saanich Road, Victoria, BC, V9E 2E7, Canada⁸ Onsala Space Observatory, Chalmers University of Technology, Observatorievägen 90, Råö, 439 92 Onsala, Sweden⁹ Department of Astronomy & Steward Observatory, University of Arizona, Tucson, AZ, USA¹⁰ Steward Observatory, 933 North Cherry Avenue, Tucson, AZ 85721, USA¹¹ Department of Astronomy, University of Florida, P.O. Box 112055, Gainesville, FL 32611-2055, USA¹² Department of Astronomy, The University of Texas, Austin, TX 78712, USA¹³ Sidrat Research, 124 Merton Street, Suite 507, Toronto, ON, M4S 2Z2, Canada¹⁴ Department of Applied Mathematics and Theoretical Physics, University of Cambridge, Cambridge, CB3 0WA, UK¹⁵ Department of Astronomy, Yale University, P.O. Box 208101, New Haven, CT 06520-8101, USA¹⁶ Korea Astronomy and Space Science Institute, 776 Daedeok-daero, Yuseong-gu, Daejeon, 34055, Republic of Korea¹⁷ Harvard-Smithsonian Center for Astrophysics, 60 Garden Street, Cambridge, MA 02138, USA¹⁸ Department of Physics and Astronomy, University of North Carolina Chapel Hill, Chapel Hill, NC 27599, USA¹⁹ Canadian Institute for Theoretical Astrophysics, University of Toronto, 60 Saint George Street, Toronto, ON, M5S 3H8, Canada²⁰ European Southern Observatory, Karl-Schwarzschild-Straße 2, 85748 Garching, Germany²¹ National Radio Astronomy Observatory, 520 Edgemont Road, Charlottesville, VA 22903, USA

Received 2024 October 10; revised 2025 September 5; accepted 2025 September 5; published 2026 January 2

Abstract

We present an overview of the final data release (DR2) from the Green Bank Ammonia Survey (GAS). GAS is a large program at the Green Bank Telescope to map all Gould Belt star-forming regions with $A_V \gtrsim 7$ mag visible from the Northern Hemisphere in emission from NH_3 and other key molecular tracers. This final release includes the data for all the regions observed: Heiles Cloud 2 and B18 in Taurus; Barnard 1, Barnard 1-E, IC 348, NGC 1333, L1448, L1451, and Per7/34 in Perseus; L1688 and L1689 in Ophiuchus; Orion A (North and South) and Orion B in Orion; Cepheus; B59 in Pipe; Corona Australis East and West; IC 5146; and Serpens Aquila and MWC297 in Serpens. Similar to what was presented in GAS DR1, we find that the NH_3 emission and dust continuum emission from Herschel correspond closely. We find that the NH_3 emission is generally extended beyond the typical 0.1 pc length scales of dense cores, and we find that the transition between coherent core and turbulent cloud is a common result. This shows that the regions of coherence are common throughout different star-forming regions, with a substantial fraction of the high column density regions displaying subsonic nonthermal velocity dispersions. We produce maps of the gas kinematics, temperature, and NH_3 column densities through forward modeling of the hyperfine structure of the NH_3 (1,1) and (2,2) lines. We show that the NH_3 velocity dispersion, σ_v , and gas kinetic temperature, T_K , vary systematically between the regions included in this release, with an increase in both the mean value and spread of σ_v and T_K with increasing star formation activity. The data presented in this paper are publicly available via doi:10.11570/24.0091.

Unified Astronomy Thesaurus concepts: Star formation (1569); Interstellar molecules (849); Astrochemistry (75)

Materials only available in the online version of record: figure set, machine-readable table

1. Introduction

Stars form in molecular cores, the densest parts of molecular clouds, which provide the initial conditions for star formation (J. E. Pineda et al. 2023). Key properties providing information about core evolution are density, temperature, velocity, and degree of turbulence. Dense cores can be efficiently identified in dust continuum emission, since it is a good tracer of the total gas

²² Jansky Fellow of the National Radio Astronomy Observatory.



column density. Though such observations have resulted in catalogs of dense cores, they do not probe the gas kinematics.

Observations of dense cores in molecular lines are extremely useful, since they provide complementary information about the chemistry and kinematics of cores. Typical dense core tracers, such as NH_3 and N_2H^+ , are commonly used, since they hardly deplete from the gas phase (A. Crapsi et al. 2007; E. Redaelli et al. 2019; P. Caselli et al. 2022; J. E. Pineda et al. 2022; Y. Lin et al. 2023). On the other hand, tracers such as C^{18}O or C_2S are useful to study a different environment than the dense gas tracers lines. Chemical models predict that species such as C_2S , HC_5N , and HC_7N have a peak in abundance at earlier times than species such as NH_3 or N_2H^+ (H. Suzuki et al. 1992; Y. Aikawa et al. 2001), and carbon-bearing species are more affected by molecular depletion (P. Caselli et al. 1999; M. Tafalla et al. 2002). It is for these two reasons that the two groups of molecules appear to trace different volumes.

Thanks to its metastable levels, NH_3 can serve as an efficient thermometer (P. T. P. Ho & C. H. Townes 1983; C. M. Walm-sley & H. Ungerechts 1983). In addition, the hyperfine structures of the NH_3 lines enable a precise study of the kinematic information. Hence, NH_3 is widely used to determine dense core properties (P. C. Myers & P. J. Benson 1983; R. Bachiller & J. Cernicharo 1986; P. J. Benson & P. C. Myers 1989; J. Jijina et al. 1999; M. Tafalla et al. 2004; Y. Wu et al. 2006; E. W. Rosolowsky et al. 2008; J. E. Pineda et al. 2010; C. R. Purcell et al. 2012; M. Wien et al. 2012; Y. M. Seo et al. 2015; O. Fehér et al. 2016).

The Gould Belt clouds include the nearby clouds (<1 kpc), which have been studied in great detail with different observatories. The protostellar content is well determined with Spitzer observations (M. M. Dunham et al. 2015), the Herschel observations provide maps of the total column density, $N(\text{H}_2)$, and dust temperature, while ground-based observations with SCUBA2 at the JCMT provide the dense core catalogs.

The initial data release, Green Bank Ammonia Survey (GAS) DR1, provided fully reduced data cubes for all lines observed, NH_3 (1,1), (2,2), and (3,3), C_2S , HC_5N , and HC_7N , as well as the derived parameters of fitting the NH_3 (1,1) and (2,2) lines for a limited number of regions (R. K. Friesen et al. 2017). In this second release, we now include all regions observed, as well as the derived parameters for the carbon-bearing species (C_2S , HC_5N , and HC_7N). All data and the corresponding derived parameters are delivered as FITS files via CANFAR at doi:10.11570/24.0091.

GAS DR1 data have been used to examine the structure and kinematics of dense gas within the nearby star-forming regions. An incomplete list of findings includes the following: (a) the smallest cores identified in GAS tend not to be bound by gravity but are instead pressure confined (J. Keown et al. 2017; H. Kirk et al. 2017; R. Kerr et al. 2019), while larger molecular clumps appear virialized (A. Singh et al. 2021); (b) multiple velocity components in the NH_3 line profiles trace supersonic gas around subsonic cores in L1688 (S. Choudhury et al. 2020), and the quiescent core gas extends further out than previously argued (S. Choudhury et al. 2021); (c) velocity gradients within cores and filaments suggest mass accretion onto and along filaments (M. C.-Y. Chen et al. 2020); and (d) core shapes and velocity gradients are generally randomly oriented with respect to the large-scale magnetic field traced by Planck (C.-Y. Chen et al. 2020; A. Pandhi et al. 2023).

In this paper, we present the full GAS dataset. In Section 2, we describe the observations, and calibration and gridding of the data. In Section 3, we describe the line fitting, moment maps, and column density calculations for all observed lines. In Section 4, we discuss the bulk variation of some of the dense gas properties, and examine the use of carbon-chain versus NH_3 emission to identify and analyze mass accretion via streamers in Perseus B1. We summarize our results in Section 5 and provide links to the final dataset.

2. Observations and Data

The GAS survey's goals were to map all regions with visual extinctions $A_V \gtrsim 7$ mag toward the Northern Hemisphere-visible molecular clouds in the Gould Belt. The value of $A_V \sim 7$ mag is motivated by a possible column density threshold for dense cores (e.g., D. Johnstone et al. 2004; P. André et al. 2010) and by detectability of NH_3 in previous observations. This selection comprises many of the star-forming clouds within ~ 500 pc of the Sun, covering a range in cloud sizes, masses, and star formation activity. Table 1 lists the regions observed along with their distances and area mapped per region. Overall, GAS mapped ~ 4 deg² on sky over nine clouds with distances ranging from ~ 120 to ~ 400 pc, with one cloud (IC 5146) at a distance of ~ 800 pc. An example of the coverage in Perseus is shown in Figure 1, which includes Barnard 1, Barnard 1E, NGC 1333, Per7/34, L1448, and L1451.

Observations for the GAS survey were performed from 2015 January through 2016 March at the Robert C. Byrd Green Bank Telescope (GBT) using the 7 pixel K-band Focal Plane Array (KFPA) and the Versatile GBT Astronomical Spectrometer (VEGAS). Observational details were first presented in GAS DR1, which focused on the NH_3 (1,1) and (2,2) emission from four regions. We refer the reader to GAS DR1 (R. K. Friesen et al. 2017) for a full description of the observations, data reduction, and imaging of the survey data. Here, we primarily discuss observations of the additional spectral lines and targeted regions, as well as improvements to the GAS data reduction pipelines that are utilized in the data release associated with this paper.

The VEGAS backend was used in its configuration Mode 20, allowing eight spectral windows per KFPA beam, each with a bandwidth of 23.44 MHz and 4096 spectral channels. The resulting spectral resolution of 5.7 kHz gives a velocity resolution of ~ 0.07 km s⁻¹ at 23.7 GHz. The GAS setup used six of eight available spectral windows to target six spectral lines in each beam: the NH_3 (1,1) through (3,3) inversion transitions, plus the HC_5N and HC_7N rotational transitions listed in Table 2. In addition, the C_2S $2_1 - 1_0$ transition (also in Table 2) was observed in a single, central beam. In-band frequency switching with a frequency throw of 4.11 MHz was used, maximizing the observing time spent on-source.

Observations were done in on-the-fly (OTF) mode, most often scanning in R.A. or decl. over square regions of size $10' \times 10'$. The observed coverage of most regions consists of multiple such observing blocks to cover the desired area, generally observed on different dates. Most $10' \times 10'$ blocks were observed once to reach the survey's sensitivity goals, but several were observed twice to mitigate the effects of poor weather in the first observations. In some regions, maps of $5' \times 10'$ were better suited to match the expected emission structure. Toward a few regions, the maps (and scan direction)

Table 1
Observed Regions, Distances, and Masses

Cloud	Region	Distance (pc)	Area (deg ²)	Mass (M_{\odot})	References
Taurus	HC2	138.6	0.35	271	(1)
Taurus	B18	126.6	0.33	209	(1)
Perseus	L1451	279	0.08	123	(2)
Perseus	L1448	288	0.08	162	(2)
Perseus	L1455	279	0.08	177	(2)
Perseus	NGC 1333	299	0.25	590	(2)
Perseus	B1	301	0.15	363	(2)
Perseus	B1E	301	0.03	42	(2)
Perseus	IC 348	321	0.14	329	(3)
Perseus	Per7/34	301	0.03	38	(2)
Ophiuchus	L1688	138.4	0.38	312	(4)
Ophiuchus	L1689	144.2	0.11	107	(4)
Ophiuchus	L1712	144.2	0.03	16	(4)
OrionA	Orion A	397	0.39	2916	(5)
OrionA	Orion A-S	428	0.19	1995	(5)
OrionB	NGC 2023	403	0.17	778	(6)
OrionB	NGC 2068	417	0.12	90	(6)
IC 5146	...	813	0.17	389	(7)
CrA	CrA East	154	0.03	8	(7)
CrA	CrA West	154	0.06	25	(7)
Pipe	B59	163	0.03	22	(7)
Pipe	Core 40	163	0.01	59	...
Serpens	Serpens Aquila	436	0.35	3141	(3)
Serpens	MWC 297	436	0.03	262	(3)
Cepheus	L1228	346	0.10	228	...
Cepheus	L1251	346	0.24	473	(8)

Notes. The mass listed is the total mass within the extent of the area mapped by GAS, calculated from dust continuum opacity and temperatures maps derived from spectral energy distribution fitting of submillimeter continuum data at similar resolution to the NH_3 observations (A. Singh & P. G. Martin 2022).

References. (1) P. A. B. Galli et al. (2018), (2) C. Zucker et al. (2018), (3) G. N. Ortiz-León et al. (2018a), (4) G. N. Ortiz-León et al. (2018b), (5) J. E. Großschedl et al. (2018), (6) M. Kounkel et al. (2018), (7) S. A. Dzib et al. (2018), (8) Q.-Z. Yan et al. (2019).

were tilted relative to the R.A. and decl. axes. In OTF mode, scans were separated by $13''$ perpendicular to the scan direction to ensure Nyquist sampling (the beam is $\approx 32''$ at these frequencies). The telescope scan rate was 6.2 s^{-1} , with data dumped every 1.044 s. Each $10' \times 10'$ map was completed in 1.4 hr. Pointing updates were usually performed in between completed maps, or more frequently if winds were high ($> 5 \text{ m s}^{-1}$).

Calibration was performed using observations of the Moon and Jupiter, following the description in GAS DR1. Individual beam gains were determined per semester and applied to the data through the GAS calibration pipeline. The calibration pipeline is essentially the same as described in GAS DR1, with improved flagging of scans with outlying T_{sys} values that improved the overall noise properties of the maps. The imaging pipeline is as described in GAS DR1. All GAS data reduction and imaging codes are publicly available on GitHub.²³

The noise properties of the data will be discussed further in Appendix A, since we used the results of the line fitting to refine the windows where the rms noise properties were

calculated. We note here, however, that the C_2S emission maps have a factor $\sim \sqrt{7}$ higher rms noise, along with a smaller map footprint relative to lines observed with all seven KFPA beams due to being observed in a single beam only. In addition, the spectral window targeting the HC_7N (22–21) line often showed greater noise values than the others. Finally, the spacing of the KFPA beams results in increased rms noise values at the map edges for the other lines. We masked the final data cubes by performing a binary erosion with a two-dimensional disk of three pixels diameter on the combined map, in addition to removing the images' edges prior to any further analysis.

3. Analysis

The calibration and imaging pipelines described above produce data cubes in position–position–velocity space. In regions larger than the typical $10' \times 10'$ observational footprint, map blocks are combined to cover contiguous areas toward each observed region. Table 1 lists the total map area observed for each region; regions with areas greater than 0.03 deg^2 contain multiple blocks.

3.1. Line Fitting

3.1.1. Hyperfine Model Fitting of NH_3 (1,1) and (2,2)

Following the method described in GAS DR1, we fit simultaneously the NH_3 (1,1) and (2,2) lines using the `cold ammonia` model implemented in `pyspeckit` (A. Ginsburg & J. Mirocha 2011; A. Ginsburg et al. 2022). From the simultaneous fits, we obtain five fit parameters: v_{LSR} , σ_v , T_{K} , T_{ex} , and $N(\text{NH}_3)$. We note that T_{K} is derived assuming the filling factor is unity and the relation between rotational temperature and kinetic temperature derived by J. J. Swift et al. (2005), which assumes that both transitions have the same excitation temperature and velocity dispersion. We follow the masking rules adopted in GAS DR1 (see R. K. Friesen et al. 2017, for details) to only keep fitted parameters with a reliable determination.

3.1.2. Single Gaussian Fitting of NH_3 (3,3) and Carbon-bearing Species CCS , HC_3N , and HC_7N

The NH_3 (J, K) transitions observed here are inversion transitions, where J is the total angular momentum quantum number, and K is the component of J along the molecular axis. NH_3 (3,3) is an ortho- NH_3 transition ($K = 3n$, where $n = 0, 1, 2, \dots$), whereas NH_3 (1,1) and (2,2) are transitions of para- NH_3 ($K \neq 3n$). The para- and ortho- NH_3 states are not well connected in typical conditions in dense clouds, and we thus treat NH_3 (3,3) as a separate species. While the line is also an inversion transition and contains hyperfine structure as the NH_3 (1,1) and (2,2) transitions, we do not detect it with sufficient signal-to-noise ratio (S/N) to detect the separate components, and consequently fit the line with a single Gaussian.

For NH_3 (3,3) and each carbon-bearing species and transition, we fit all spectra with $\text{S/N} > 3$ with a single Gaussian component, producing maps of line amplitude, T_B , line-of-sight velocity in the local standard of rest frame, v_{LSR} , and Gaussian line width, σ_v , along with their respective uncertainties. The parameter maps were masked where the uncertainty in v_{LSR} was greater than 0.3 km s^{-1} , and where σ_v

²³ <https://GitHub.com/GBTAmmoniaSurvey/GAS>

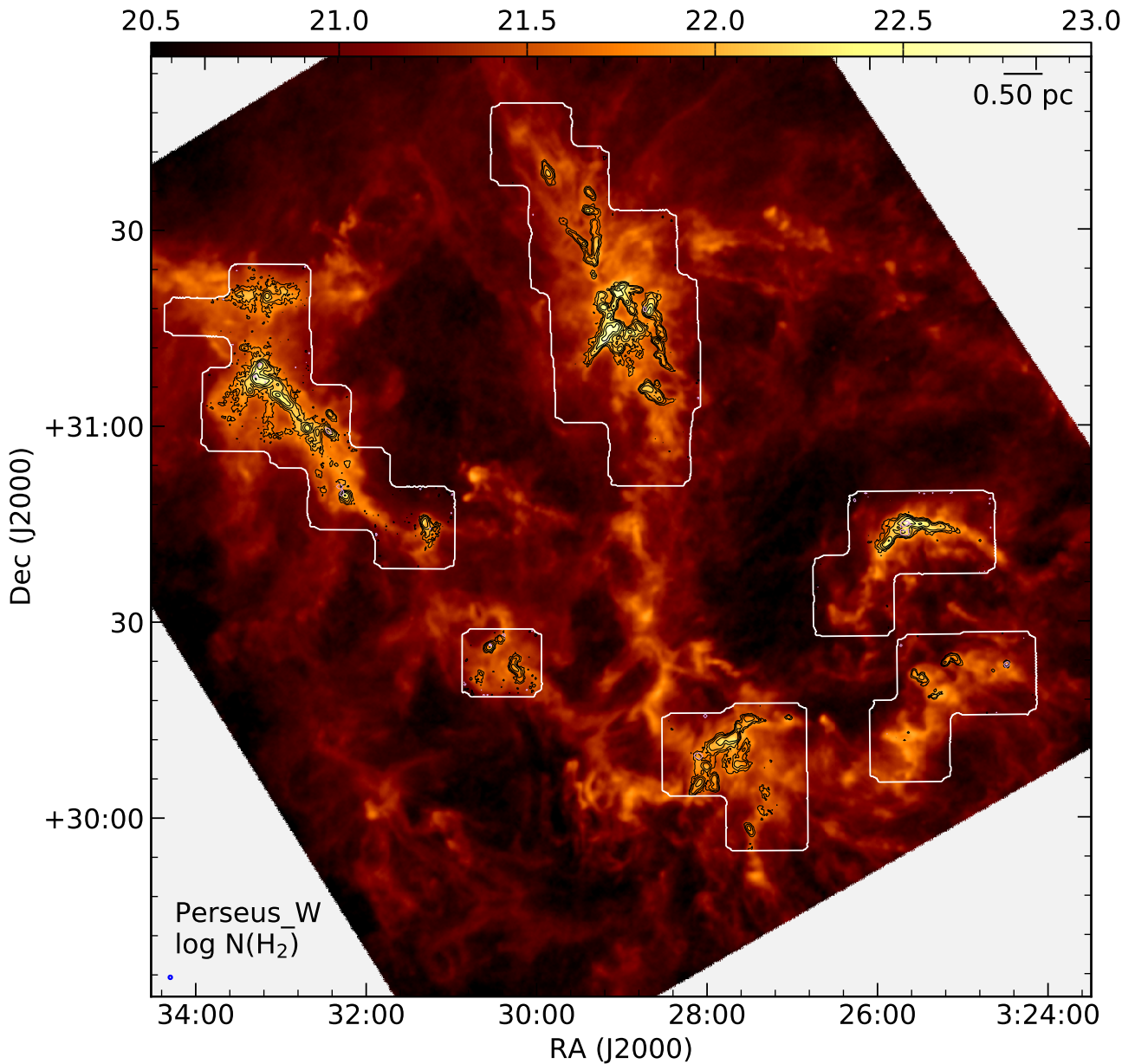


Figure 1. Observed GAS regions in the western Perseus molecular cloud. The color scale shows $N(\text{H}_2)$ derived from spectral energy distribution fitting of Herschel continuum maps (A. Singh & P. G. Martin 2022). White contours highlight the extent of the GAS maps. Black contours show the integrated NH_3 (1,1) emission. The $32''$ GBT beam is shown at bottom left.

Table 2
Line Parameters

Species	Transition	ν (GHz)	B_0 (MHz)	μ (Debye)
HC_5N	$J = 9-8$	23.963901	1331.33	4.33
HC_7N	$J = 21-20$	23.6878974	564.0	4.82
HC_7N	$J = 22-21$	24.8158772	564.0	4.82
C_2S	$J_N = 2_1-1_0$	22.344030	6477.75	2.88

was less than 3 times its fit uncertainty. Finally, we masked pixels without neighboring good fits.

Following the method described in more detail in GAS DR1, we use the v_{LSR} and σ_v results of the line fits to identify the windows where we compute the noise properties of the cubes. We show in Figure 2 the resulting integrated intensity maps of NH_3 (1,1), C_2S , HC_5N , and HC_7N toward Heiles Cloud 2.

We detect NH_3 (3,3) above the S/N threshold toward six regions: L1688, NGC 1333, Orion A, NGC 2023-2024, and NGC 2067-2071 in Orion B, and Serpens Aquila. The emission is clearly associated with regions impacted by feedback from young intermediate or high-mass stars. In L1688, the emission is extended along and to the west of the Oph A clump, sometimes called ρ Oph West (A. Abergel et al. 1996), illuminated by the early B star HD 147889. In NGC 1333, NH_3 (3,3) is compact and located near the SVS 13 region, a hierarchical system of four protostellar sources (X. Chen et al. 2009), at least one of which is driving a large-scale chain of Herbig–Haro objects (R. Chini et al. 1997). NH_3 (3,3) is strongly detected toward Orion KL and Orion A-S, with extended emission along the Orion Bar and north along the integral-shaped filament. Within NGC 2024, we find NH_3 (3,3) near the young high-mass stars IRS2 and IRS2b. Toward Serpens Aquila, NH_3 (3,3) highlights multiple filamentary features seen in submillimeter continuum observations near

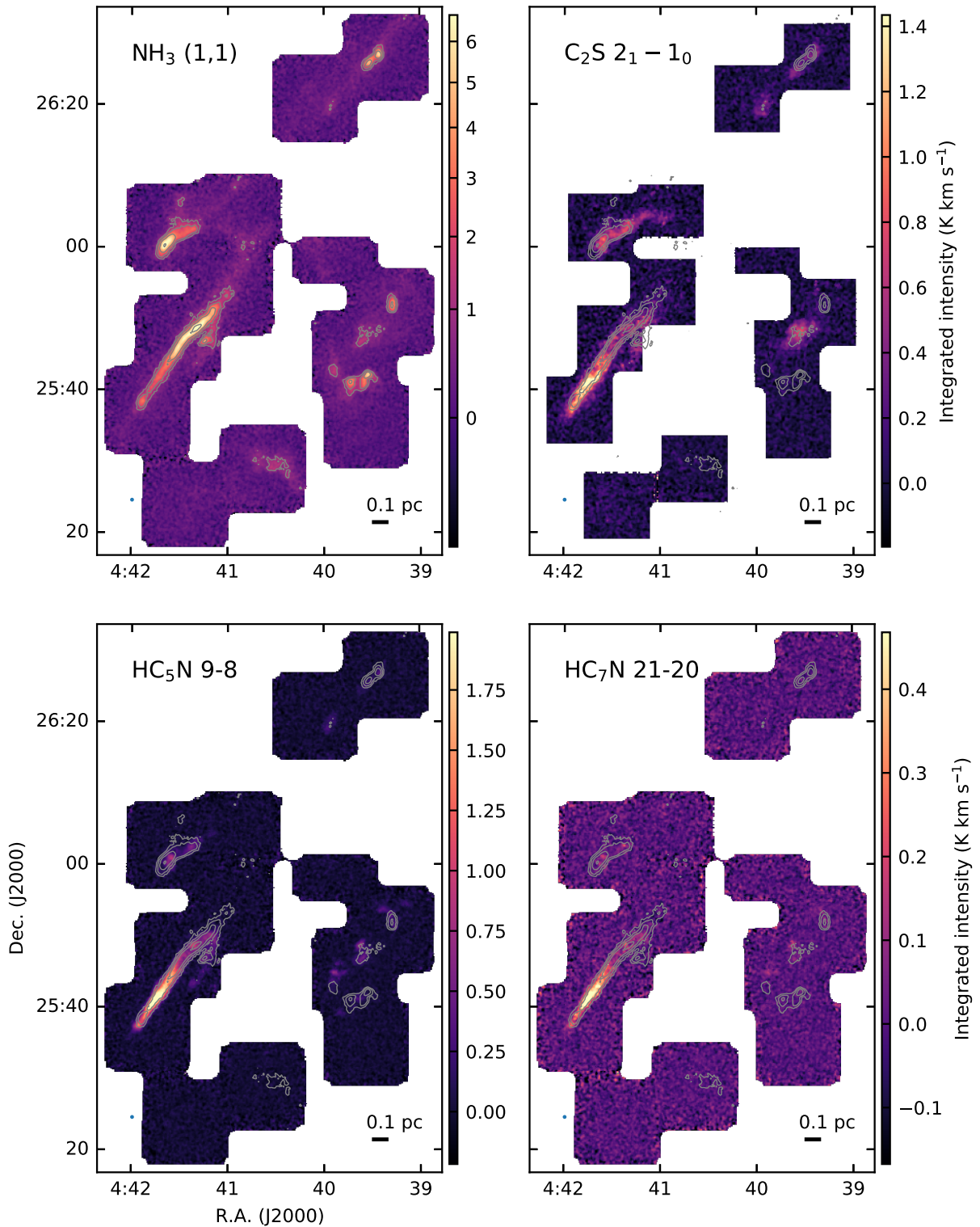


Figure 2. Integrated intensity of NH_3 (1,1), C_2S , HC_5N , and HC_7N emission toward Heiles Cloud 2 in Taurus. In all plots, gray contours follow the NH_3 (1,1) emission. The blue circle at lower left shows the GBT beam.

the center of the W40 HII region (G. Westerhout 1958; K. K. Mallick et al. 2013).

3.2. Column Densities of C_2S , HC_5N , and HC_7N

For NH_3 , column density calculations are presented in GAS DR1 based on modeling of the (1,1) and (2,2) inversion transitions. In this release, we present the NH_3 column density

maps of all regions in the GAS survey, including those presented in DR1. Here, we determine the column densities for the additional species C_2S , HC_5N , and HC_7N where detected in the GAS survey. Table 2 lists the rotational transitions and parameters for each line observed.

We use the resulting fit line brightness and velocity dispersion in the following column density derivation. All

three species are linear molecules. We therefore follow J. G. Mangum & Y. L. Shirley (2015) to derive the total molecular column density, N_{tot} , for rotational transitions $J_u \rightarrow J_u - 1$ at frequency ν for optically thin lines, where

$$N_{\text{tot}} = \frac{3h}{8\pi^3 S_{i,j} |\mu|^2} \frac{Q_{\text{rot}}}{g_u} \frac{\exp\left(\frac{E_u}{kT_{\text{ex}}}\right)}{\exp\left(\frac{h\nu}{kT_{\text{ex}}}\right) - 1} \int \tau_\nu dv. \quad (1)$$

Here, τ_ν is the opacity as a function of frequency ν . For these species, the associated line strength $S_{i,j} = J_u^2 / (2J_u + 1)$, the rotational degeneracy $g_u = 2J_u + 1$, and $E_u = hB_0 J_u(J_u + 1)$ is the energy above ground state. For HC₅N and HC₇N, we calculate the rotational partition function, Q_{rot} , following the approximation (R. S. McDowell 1988)

$$Q_{\text{rot}} \simeq \frac{kT}{hB_0} \exp(hB_0/3kT), \quad (2)$$

which is accurate to 0.01% when $hB_0/kT \lesssim 0.2$. For C₂S, we evaluate $Q_{\text{rot}} = \sum g_u \exp(-E_u/kT_{\text{ex}})$ over all $E_u/k < 1000$ K. For each species, the dipole moment μ and rotational constant B_0 were taken from the Spectral Line Atlas of Interstellar Molecules²⁴ (A. J. Alexander et al. 1976; H. W. Kroto et al. 1978; S. Saito et al. 1987, for HC₅N, HC₇N, and C₂S, respectively).

The integral over the opacity per frequency, $\int \tau_\nu dv$, can be simplified to $\sqrt{2\pi} \sigma_v \tau$, where σ_v is the velocity dispersion of the emission line assuming a Gaussian profile, and

$$\tau = -\ln \left[1 - \frac{T_B}{J(T_{\text{ex}}) - J(T_{\text{bg}})} \right], \quad (3)$$

is the peak opacity of the emission line. Here, $J(T) \equiv h\nu/k_B (\exp(h\nu/k_B T) - 1)$ is the Rayleigh–Jeans equivalent temperature, T_B is the peak line brightness temperature, T_{ex} is the excitation temperature, and $T_{\text{bg}} = 2.73$ K is the background temperature.

We set $T_{\text{ex}} = 7$ K for all regions and all carbon-bearing species, with the exception of Heiles Cloud 2 in Taurus, where S. E. T. Smith et al. (2023) determine $T_{\text{ex}} = 8.4$ K is more appropriate for HC₅N in TMC-1 using GAS data. Given the range of line brightness temperatures T_B and velocity dispersions σ_v where the carbon-bearing species are detected, we find that varying the assumed T_{ex} between 5 and 10 K produces an overall variation in the resulting column densities of $\lesssim 0.2$ dex in all species. Given that we do not have strong constraints on T_{ex} , we conclude this is our typical uncertainty in the reported values.

3.3. Molecular Abundances and Region Masses

The clouds observed with GAS were also mapped by the Herschel Gould Belt Survey (HGBS; P. André et al. 2010) in continuum emission from dust with both PACS (70 and 160 μm ; A. Poglitsch et al. 2010) and SPIRE (250, 350, and 500 μm ; M. J. Griffin et al. 2010). A. Singh & P. G. Martin (2022) produced standardized modified blackbody fits of the spectral energy distribution across the HGBS clouds, producing maps of the dust opacity τ and temperature T_d at

36'' resolution (the angular resolution of Herschel in the 500 μm passband).²⁵ We calculate the column density of H₂, $N(\text{H}_2)$, following

$$\tau_\nu = \kappa_\nu R_d \mu_{\text{H}_2} m_{\text{H}} N(\text{H}_2) \quad (4)$$

(A. Singh & P. G. Martin 2022, Appendix D), where κ_ν is the dust emission cross section per unit mass as a function of frequency ν , τ_ν is the dust opacity as a function of ν , R_d is the dust to gas mass ratio, m_{H} is mass of the hydrogen atom, and $\mu_{\text{H}_2} = 2.8$ (J. Kauffmann et al. 2008). To calculate $N(\text{H}_2)$, we set $\kappa_\nu = 10 \text{ cm}^2 \text{ g}^{-1}$ at $\nu = 1$ THz, matching A. Singh & P. G. Martin (2022), and $R_d = 0.01$. Because the angular resolution of the GAS and $N(\text{H}_2)$ maps thus derived are very similar (32'' and 36'', respectively), we assume that the column density maps are smooth at these angular scales and therefore regrid the resulting $N(\text{H}_2)$ maps to match the GAS data. We are then able to determine per-pixel molecular abundances given the fit results of the various lines observed and $N(\text{H}_2)$. We further calculate the total mass within the GAS mapped regions based on the $N(\text{H}_2)$ maps and the distances to each region, and show the results in Table 1.

3.4. NH₃ and Continuum Crossmatched Core Properties

A. Pandhi et al. (2023) used dendrogram analysis to identify dense molecular cores in integrated NH₃ (1,1) emission across most of the observed GAS clouds. They then crossmatch the NH₃-detected structures with core catalogs derived from submillimeter observations to produce a catalog of NH₃ cores that coincide with submillimeter cores, and we refer the reader to A. Pandhi et al. (2023) for a detailed description of the core identification and matching analysis. Using the crossmatched catalog, A. Pandhi et al. (2023) measure velocity gradients across the cores, examine the specific angular momentum as a function of core size, and show that the relative orientations of the cores, their specific angular momentum vectors, and the large-scale magnetic field as traced by Planck show little to no evidence for preferred alignment or antialignment.

Here, we provide the mean and standard deviation of the gas properties derived from the NH₃ line fits measured within the NH₃ core boundaries for the crossmatched cores from A. Pandhi et al. (2023). We additionally calculate the virial parameter $\alpha_{\text{vir}} = M_{\text{vir}}/M$ for each core, where M is the continuum core mass. We define M_{vir} following F. Bertoldi & C. F. McKee (1992):

$$M_{\text{vir}} = \frac{5\sigma^2 R}{a G}, \quad (5)$$

where R is the core radius, G is the gravitational constant, σ is the total clump velocity dispersion, and a is a factor that depends on the density profile of the core. For each core, we set R equal to the continuum catalog core radius, and we set $a = 1$ (A. Singh et al. 2021), which corresponds to a uniform density while for a free-falling core ($\rho(r) \propto r^{-1.5}$) $a = 1.25$. The total clump velocity dispersion takes into account both the mean line width (given as σ_v) and the dispersion of the mean

²⁴ <https://www.splatalogue.online>

²⁵ <https://www.cita.utoronto.ca/HOTT/>

line-of-sight velocity, σ_{vlsr} , across the core

$$\sigma^2 = \sigma_{\text{vlsr}}^2 + \sigma_v^2 - \frac{k_B T_K}{m_{\text{NH}_3}} + \frac{k_B T_K}{\mu m_H}, \quad (6)$$

where we remove the NH_3 thermal line width and include the thermal line width of the mean gas, T_K is the mean kinetic temperature over the core, k_B is the Boltzmann constant, m_{NH_3} is the molecular mass of ammonia, m_H is the molecular mass of hydrogen, and $\mu = 2.37$ for molecular gas (J. Kauffmann et al. 2008). This procedure calculates the nonthermal component of the core by removing the thermal velocity dispersion of the NH_3 line (e.g., J. E. Pineda et al. 2021; R. K. Friesen & E. Jarvis 2024). The first term, σ_{vlsr} , estimates the dense core bulk motion, which arises from variations of the line-of-sight velocity corresponding to internal motions (see A. Singh et al. 2021). Finally, it adds the thermal velocity dispersion for the average particle, which represents the thermal support within the dense core. Given M_{vir} for each core, we then calculate α_{vir} .

A short version of this core property catalog is shown in Table 8, while the full version is available online.

4. Discussion

4.1. NH_3 Fit Results across Regions

Based on the NH_3 line fits, we identify several broad trends in the dense gas properties across the GAS clouds. For each region and fit parameter (v_{LSR} , σ_v , T_{ex} , T_K , and $N(\text{NH}_3)$), we list in Table 3 the 50th percentile, as well as the 16th and 84th percentiles, of the distributions of fit parameters toward each observed region. We report percentiles rather than mean and 1σ values as the distributions are not necessarily Gaussian. We mask fit parameters based on the uncertainties in the NH_3 fits following GAS DR1. We additionally show in Figure 3 the distribution of NH_3 fit parameters for the observed regions as violin plots. In these plots, the top and bottom bars show the maximum and minimum values for each parameter, while the mean and median values are shown as horizontal bars within the distribution. The fraction of pixels with a given parameter value is highlighted by the width of the violin. The regions are ordered from left to right and also color coded by increasing mean gas temperature T_K , shown in the middle panel. For regions where fewer than 10 pixels have T_K measurements after masking, we set the mean $T_K = 10$ K.

For most regions, v_{LSR} falls between ~ 0 and $\sim 12 \text{ km s}^{-1}$, with the exception of the two Cepheus clouds. While most regions do show a distribution of at least several km s^{-1} in v_{LSR} across the mapped areas, most of the gas often lies in a narrow v_{LSR} range (with the exception of Orion A, and to a lesser extent NGC 2023-2024 in Orion B). Regions with very little spread in v_{LSR} tend to be those with small mapped areas.

Toward all regions, the observed velocity dispersion, σ_v , varies from very low, subsonic values to supersonic, but the ranges in σ_v values and the distribution change between regions. Figure 3 shows that the variation in σ_v is clearly correlated with increased T_K , see also Appendix D for a direct comparison. Colder regions tend to have a larger fraction of the dense gas with smaller σ_v , whereas warmer regions show an increasing fraction of the dense gas with larger line widths. We note that all regions still contain gas at very low σ_v , but

these regions tend to be limited to compact cores in, e.g., Orion A, rather than being broadly extended.

Gas temperatures vary across the observed clouds, with median values ranging from ~ 9 K (e.g., HC2 in Taurus) to ~ 16 K (e.g., Orion A and B). In general, regions that are colder on average also show a smaller spread in T_K across the mapped area. While all regions still contain some fraction of the mapped area with very low σ_v , even when the mean value is higher, warmer regions do not necessarily retain similarly cold gas as those regions that are colder on average. Minimum gas temperatures, even in compact cores with low σ_v values, are higher by several K in regions such as Orion A compared with regions in Taurus.

In contrast to σ_v and T_K , both T_{ex} and $N(\text{NH}_3)$ show similar variation and spread across most of the regions. Mean T_{ex} values tend to lie within ~ 4 – 5 K, with spreads of a few kelvin.

We further include in Table 3 the median and (16th, 84th) values for the nonthermal velocity dispersion σ_{NT} , and the NH_3 abundance relative to H_2 , $X(\text{NH}_3)$. At each pixel where both σ_v and T_K are fit well, we calculate σ_{NT} following

$$\sigma_{\text{NT}} = \left(\sigma_v^2 - \frac{k_B T_K}{m_{\text{NH}_3}} \right)^{1/2}, \quad (7)$$

where m_{NH_3} is the molecular weight of NH_3 .

We determine $X(\text{NH}_3) = N(\text{NH}_3)/N(\text{H}_2)$ at each pixel where $N(\text{NH}_3)$ is fit well, using the $N(\text{H}_2)$ maps described in Section 3.3. We find that the individual region's average abundance, $\log_{10} X(\text{NH}_3)$, is between -7.7 and -8.2 , and a typical value of -8.0 is seen across all the clouds. This value is consistent with previous observations of dense cores (M. Tafalla et al. 2004; R. K. Friesen et al. 2009; J. E. Pineda et al. 2022); however, these observations do not have sufficient angular resolution to resolve possible NH_3 depletion as seen in other objects (P. Caselli et al. 2022; J. E. Pineda et al. 2022; Y. Lin et al. 2023).

4.2. Appearance of Subsonic Structures

In the past, several works showed the presence of a transition to coherence, where the nonthermal velocity dispersion transitions from supersonic values in the molecular cloud down to subsonic values in the dense core (A. A. Goodman et al. 1998; J. E. Pineda et al. 2010; A. Hacar et al. 2018; H. H.-H. Chen et al. 2019; S. Choudhury et al. 2021). We compare the velocity dispersion as a function of H_2 column density for all regions in Figure 4. We use the kernel density estimation (KDE) implementation in *scipy* (P. Virtanen et al. 2020), while in regions with fewer than 100 detections, we plot the individual data points. The regions shown in Figure 4 are sorted by increasing mean kinetic temperature, T_K , while the expected velocity dispersion for $\mathcal{M}_s = \sigma_{\text{NT}}/c_s$ equal 1 and 0.5 are marked by the red-dotted and black-dashed horizontal lines, respectively. This figure shows that there is no *universal column density* at which the level of nonthermal velocity dispersion is subsonic.

Furthermore, we compute the KDE of the effective radius and the minimum column density for all subsonic structures. Independent structures are identified in the images using *scipy.ndimage.label*, and only those with at least 10 pixels are retained. For each structure, we determine the effective radius and the minimum H_2 column density, and then calculate the KDE across all regions. The radius distribution

Table 3
NH₃ Fit Results per Region

Region	v_{LSR} (km s ⁻¹)	σ_v (km s ⁻¹)	T_{ex} (K)	T_{K} (K)	$\log N(\text{NH}_3)$ (cm ⁻²)	σ_{NT} (km s ⁻¹)	$\log X(\text{NH}_3)$
B1	6.60 ^{+0.25} _{-0.20}	0.32 ^{+0.21} _{-0.15}	3.7 ^{+1.8} _{-0.7}	10.7 ^{+1.3} _{-1.0}	14.1 ^{+0.3} _{-0.2}	0.18 ^{+0.11} _{-0.06}	-8.0 ^{+0.2} _{-0.2}
B18	6.19 ^{+0.23} _{-0.29}	0.15 ^{+0.16} _{-0.06}	4.3 ^{+1.8} _{-1.2}	9.5 ^{+1.0} _{-0.8}	14.0 ^{+0.3} _{-0.2}	0.09 ^{+0.04} _{-0.02}	-8.1 ^{+0.2} _{-0.2}
B1E	7.51 ^{+0.12} _{-0.68}	0.24 ^{+0.90} _{-0.11}	3.1 ^{+0.5} _{-0.2}
B59	3.42 ^{+0.13} _{-0.14}	0.17 ^{+0.09} _{-0.03}	6.3 ^{+1.6} _{-1.5}	11.5 ^{+2.6} _{-1.6}	13.9 ^{+0.3} _{-0.3}	0.15 ^{+0.10} _{-0.04}	-8.2 ^{+0.2} _{-0.2}
Cepheus_L1228	-8.11 ^{+0.35} _{-0.17}	0.16 ^{+0.08} _{-0.03}	4.7 ^{+1.1} _{-1.0}	10.7 ^{+1.0} _{-1.2}	14.1 ^{+0.3} _{-0.2}	0.14 ^{+0.09} _{-0.03}	-8.0 ^{+0.2} _{-0.2}
Cepheus_L1251	-3.99 ^{+0.36} _{-0.67}	0.14 ^{+0.14} _{-0.04}	4.7 ^{+1.2} _{-1.2}	10.2 ^{+1.4} _{-1.0}	14.1 ^{+0.3} _{-0.3}	0.12 ^{+0.11} _{-0.03}	-8.0 ^{+0.2} _{-0.2}
CrAeast	5.66 ^{+0.09} _{-0.14}	0.18 ^{+0.10} _{-0.06}	5.1 ^{+1.2} _{-1.4}	9.6 ^{+1.8} _{-1.0}	14.2 ^{+0.2} _{-0.2}	0.14 ^{+0.03} _{-0.05}	-8.0 ^{+0.2} _{-0.2}
CrAwest	5.61 ^{+0.25} _{-0.34}	0.27 ^{+0.16} _{-0.10}	5.0 ^{+3.4} _{-1.4}	14.5 ^{+3.4} _{-2.1}	14.3 ^{+0.2} _{-0.2}	0.23 ^{+0.12} _{-0.07}	-8.1 ^{+0.2} _{-0.2}
HC2	5.69 ^{+0.57} _{-0.50}	0.14 ^{+0.20} _{-0.05}	4.3 ^{+1.5} _{-1.1}	9.4 ^{+1.3} _{-0.9}	13.9 ^{+0.3} _{-0.3}	0.08 ^{+0.05} _{-0.02}	-8.1 ^{+0.2} _{-0.2}
IC 348	8.76 ^{+0.38} _{-0.42}	0.26 ^{+0.17} _{-0.11}	3.9 ^{+1.9} _{-0.8}	11.8 ^{+2.3} _{-1.2}	14.0 ^{+0.2} _{-0.2}	0.16 ^{+0.11} _{-0.05}	-8.0 ^{+0.2} _{-0.2}
IC 5146	3.87 ^{+0.30} _{-0.27}	0.22 ^{+0.10} _{-0.09}	4.0 ^{+1.0} _{-0.7}	11.1 ^{+1.9} _{-1.5}	14.1 ^{+0.2} _{-0.2}	0.19 ^{+0.11} _{-0.07}	-7.8 ^{+0.1} _{-0.2}
L1448	4.44 ^{+0.30} _{-0.39}	0.24 ^{+0.16} _{-0.09}	5.1 ^{+1.3} _{-1.6}	10.7 ^{+1.4} _{-1.3}	14.2 ^{+0.3} _{-0.2}	0.18 ^{+0.14} _{-0.05}	-8.0 ^{+0.1} _{-0.2}
L1451	4.37 ^{+0.25} _{-0.37}	0.14 ^{+0.05} _{-0.02}	4.5 ^{+0.9} _{-0.7}	9.6 ^{+1.1} _{-1.0}	13.9 ^{+0.2} _{-0.2}	0.11 ^{+0.03} _{-0.02}	-7.8 ^{+0.2} _{-0.2}
L1455	5.14 ^{+0.29} _{-0.28}	0.21 ^{+0.17} _{-0.09}	4.3 ^{+1.5} _{-1.1}	10.6 ^{+1.5} _{-1.2}	14.0 ^{+0.2} _{-0.2}	0.12 ^{+0.09} _{-0.04}	-7.9 ^{+0.2} _{-0.2}
L1688	3.47 ^{+0.28} _{-0.22}	0.33 ^{+0.16} _{-0.14}	3.8 ^{+1.9} _{-0.6}	13.1 ^{+2.7} _{-2.4}	14.0 ^{+0.2} _{-0.2}	0.17 ^{+0.19} _{-0.08}	-8.2 ^{+0.2} _{-0.2}
L1689	4.03 ^{+0.53} _{-0.33}	0.24 ^{+0.15} _{-0.08}	4.0 ^{+2.4} _{-0.9}	12.4 ^{+1.8} _{-1.1}	14.0 ^{+0.3} _{-0.3}	0.17 ^{+0.06} _{-0.05}	-8.2 ^{+0.1} _{-0.1}
L1712	4.74 ^{+0.15} _{-0.12}	0.28 ^{+0.14} _{-0.10}	3.5 ^{+0.6} _{-0.4}	13.0 ^{+2.2} _{-2.0}	14.1 ^{+0.3} _{-0.1}	0.28 ^{+0.10} _{-0.07}	...
NGC1333	7.72 ^{+0.53} _{-0.49}	0.25 ^{+0.25} _{-0.13}	4.7 ^{+1.5} _{-1.4}	11.9 ^{+2.9} _{-1.8}	14.0 ^{+0.2} _{-0.2}	0.17 ^{+0.17} _{-0.08}	-8.0 ^{+0.2} _{-0.2}
OrionA	8.40 ^{+1.68} _{-1.26}	0.52 ^{+0.48} _{-0.27}	3.8 ^{+2.4} _{-0.8}	15.6 ^{+4.8} _{-2.9}	14.1 ^{+0.3} _{-0.2}	0.30 ^{+0.26} _{-0.13}	-8.1 ^{+0.2} _{-0.2}
OrionA_S	4.51 ^{+0.46} _{-0.62}	0.22 ^{+0.16} _{-0.09}	4.6 ^{+1.1} _{-0.8}	10.6 ^{+1.6} _{-1.2}	14.1 ^{+0.2} _{-0.2}	0.15 ^{+0.09} _{-0.06}	-8.1 ^{+0.2} _{-0.2}
OrionB_NGC2023-2024	10.15 ^{+0.78} _{-0.87}	0.41 ^{+0.25} _{-0.17}	4.6 ^{+2.2} _{-1.5}	16.0 ^{+3.5} _{-1.5}	14.0 ^{+0.2} _{-0.1}	0.26 ^{+0.17} _{-0.09}	-8.1 ^{+0.1} _{-0.1}
OrionB_NGC2068-2071	10.46 ^{+0.49} _{-0.43}	0.31 ^{+0.21} _{-0.13}	5.1 ^{+1.5} _{-1.5}	15.1 ^{+2.5} _{-3.0}	14.0 ^{+0.1} _{-0.1}	0.21 ^{+0.18} _{-0.08}	-7.9 ^{+0.1} _{-0.2}
Persesus	5.94 ^{+0.11} _{-0.09}	0.12 ^{+0.04} _{-0.02}	4.9 ^{+1.2} _{-1.2}	10.3 ^{+0.9} _{-1.2}	14.1 ^{+0.2} _{-0.2}	0.09 ^{+0.04} _{-0.03}	-7.7 ^{+0.2} _{-0.2}
Pipe_Core40	3.35 ^{+0.03} _{-0.02}	0.09 ^{+0.02} _{-0.01}	4.2 ^{+1.3} _{-0.5}
Serpens_Aquila	7.29 ^{+0.55} _{-0.74}	0.23 ^{+0.17} _{-0.10}	4.2 ^{+1.2} _{-0.9}	11.3 ^{+3.3} _{-1.7}	14.1 ^{+0.2} _{-0.2}	0.15 ^{+0.10} _{-0.05}	-7.9 ^{+0.2} _{-0.2}
Serpens_MWC297	7.09 ^{+0.10} _{-0.15}	0.16 ^{+0.08} _{-0.04}	5.3 ^{+0.9} _{-1.3}	11.6 ^{+1.2} _{-1.3}	14.2 ^{+0.1} _{-0.2}	0.14 ^{+0.06} _{-0.04}	-8.1 ^{+0.1} _{-0.1}

Note. For each parameter, the values given are the 50th (16th, 84th) percentiles. For B1E and Pipe_Core40, there are not enough pixels to calculate the percentiles; therefore, we provide only the mean value.

(Figure 5 left) shows that subsonic cores are typically compact (≈ 0.05 pc), although some extend up to 0.3 pc. Similarly, the column density distribution (Figure 5, right) exhibits a peak at $\approx 6 \times 10^{21}$ cm⁻² with a FWHM of ≈ 0.5 dex, while spanning more than one order of magnitude (1 dex). Although both properties display characteristic values, neither can be described by a universal value.

We compare the fraction of pixels displaying a $\mathcal{M}_s < 1$ in Figure 6. This fraction is determined by using the mean temperature in the cloud for all pixels with a good velocity dispersion determination. The fraction is correlated with mean T_{K} in the region, although this depends on the average density in the region and the level of star formation in the region, and it shows that quiescent areas (likely cores) are even present in active star-forming regions. This suggests that stellar feedback plays a role in the scales covered with these observations, see also R. K. Friesen & E. Jarvis (2024).

Simulations further support this interpretation. The effect of feedback is studied by K. R. Neralwar et al. (2024), where they find that cores subject to stronger feedback are generally more compact but exhibit systematically higher velocity dispersions and virial parameters, implying they are more gravitationally unbound. S. S. R. Offner et al. (2022) show that many dense structures nevertheless pass through a coherent, low-turbulence phase that is consistent with the quiescent cores identified in observations such as GAS, although not all such cores survive to form stars. Taken together, these results suggest that while feedback injects turbulence and unbinds a

large fraction of dense gas, it simultaneously permits the emergence of coherent, quiescent cores within active star-forming regions, providing a natural explanation for the subsonic pockets seen in our data.

4.3. Regions with Cyanopolyne and C₂S Detections

We detect HC₅N above an S/N = 3 toward 13 separate regions within the survey. Table 4 provides a list of the regions with significant HC₅N detection, and the 50th percentile, as well as the 16th and 84th percentiles of the column densities $N(\text{HC}_5\text{N})$ and $N(\text{H}_2)$, and the HC₅N abundance relative to H₂, $X(\text{HC}_5\text{N}/\text{H}_2)$, at the locations where HC₅N is detected. We find typical mean $N(\text{HC}_5\text{N}) \sim$ a few $\times 10^{12}$ cm⁻² and mean $X(\text{HC}_5\text{N}/\text{H}_2)$ values of a few $\times 10^{-10}$, and variations in the mean values between regions are within a factor of 10. In Table 4 we further list the 50th percentile, as well as the 16th and 84th percentiles of the column density of NH₃ and the abundance ratio $N(\text{HC}_5\text{N})/N(\text{NH}_3)$ in pixels where both lines are detected. The highest abundances of HC₅N relative to NH₃ are found in Heiles Cloud 2 in Taurus, which contains the well-studied carbon-rich TMC-1 region (e.g., H. Suzuki et al. 1992; N. Kaifu et al. 2004). Toward the other GAS-targeted region in Taurus, B18, we also see extended HC₅N emission that is only slightly lower in relative abundance than toward HC2. Overall, where HC₅N emission is detected, the abundances found are in general agreement with previous studies of low-mass star-forming regions (e.g., P. J. Benson &

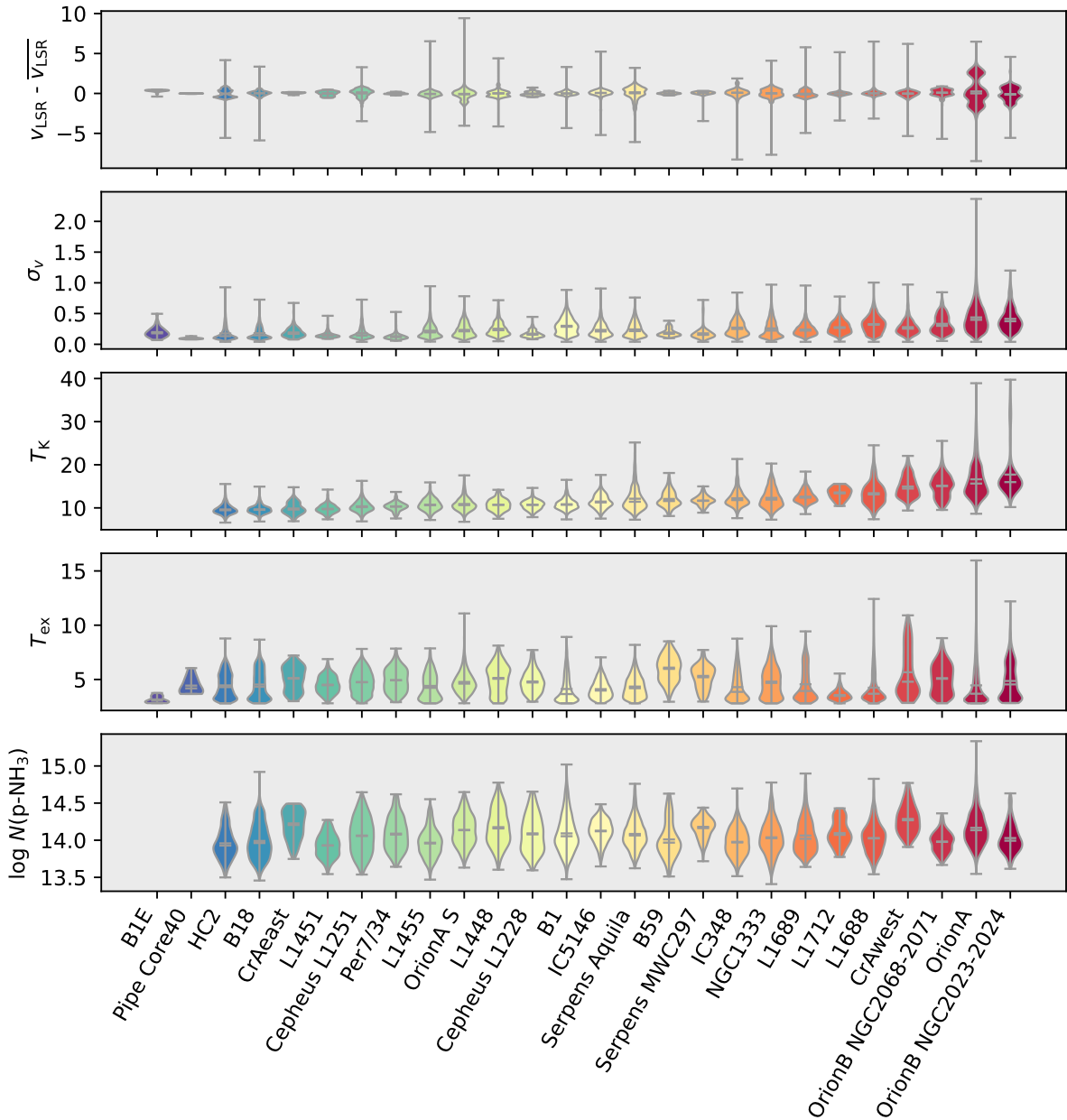


Figure 3. Fit parameter results for NH_3 (1,1) and (2,2) across all observed GAS regions. Regions are ordered by increasing mean T_K as measured by the hyperfine structure NH_3 fitting. Violin plots show the extrema, median, and mean values (horizontal lines) and the distribution of values within each region.

P. C. Myers 1983; H. Suzuki et al. 1992; C. Codella et al. 1997; T. Hirota et al. 2009). It is difficult to make direct comparisons with detailed studies of particular regions, such as TMC-1, because we observed only one HC_5N transition and thus have made simple but well-motivated assumptions about the line excitation when calculating column densities and abundances.

Of the other carbon-bearing species, we detect C_2S toward a small subset of regions where HC_5N is detected: B1 in the Perseus molecular cloud, B18 and HC2 in the Taurus molecular cloud, and Serpens Aquila. We find no detections in regions where HC_5N is not detected. As noted in Section 2, the C_2S maps have higher rms noise values, which likely limited the number of regions with detections. The cyanopolyne HC_7N was only detected toward B1, HC2, and Orion A in the $J = (21-20)$ line, and toward HC2 only in the

$J = (22-21)$ line. We present similar abundance results as in Table 4 for C_2S and HC_7N in Appendix B, where detected.

HC_5N and C_2S emission is detected in both extended and compact (approximately beam-sized) features within the different regions. These differences in morphology may point to the molecules' origins in the cold, dense gas in some locations, as well as through warm carbon-chain chemistry near protostellar sources in others. To highlight the varying distributions of the molecular tracers in one region, Figure 2 shows the integrated intensity maps for NH_3 (1,1), CCS , HC_5N , and HC_7N toward Heiles Cloud 2, containing the TMC-1 filament. Here, we have overlaid NH_3 (1,1) integrated intensity contours on the emission maps of the carbon-bearing species to compare their distributions better. The offset between the cyanopolyne and NH_3 peaks in TMC-1 is well known (L. T. Little et al. 1979), but the figure shows that much

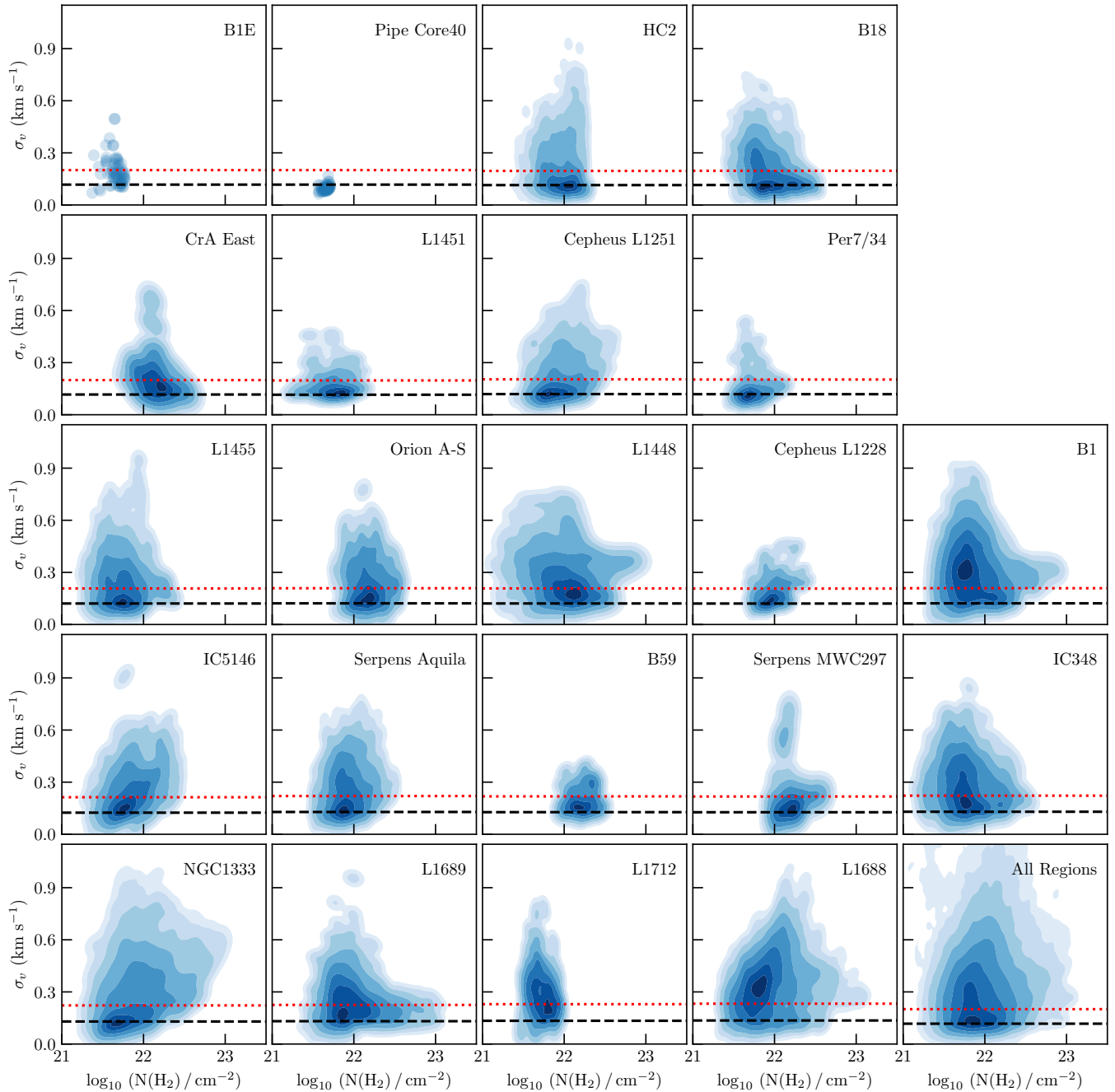


Figure 4. KDE of velocity dispersion as a function of H_2 column density for all regions covered. The red-dotted and black-dashed lines correspond to the expected velocity dispersion, σ_v , in the case of \mathcal{M}_s equals 1 and 0.5, respectively, for the median T_K value of each region. In the case of B1E, Pipe Core 40, and “All Regions,” we assume a temperature of 10 K. Notice that since the regions are already sorted by the typical kinetic temperature, the horizontal lines have only a small variation between neighboring panels.

of the extended carbon-chain emission elsewhere in the region frequently lies close to extended NH_3 emission, but offset from NH_3 emission peaks. In contrast, compact, bright HC_5N emission that is spatially coincident with compact NH_3 emission is seen toward the L1451 region, specifically toward the L1451-west source previously identified in N_2H^+ emission (S. Storm et al. 2016). S. Storm et al. (2016) argue that L1451-west is a highly evolved core that is potentially still starless. In this scenario, however, we expect much of the carbon-bearing species to be frozen out onto dust grains, which is difficult to reconcile with the bright HC_5N emission. Nevertheless, at the

resolution of the GAS observations, the source has a mean $T_K = 9.6$ K, making this an interesting and enigmatic core. We do not detect CCS or HC_7N at this location.

In some regions, spatial and kinematic offsets between the carbon-chain species and NH_3 have been explained in terms of relative dynamical ages (e.g., TMC-1; H. Suzuki et al. 1992), and as tracers of mass infall or accretion onto molecular filaments (R. K. Friesen et al. 2013; S. E. T. Smith et al. 2023). A detailed region-by-region analysis of these features is beyond the scope of this paper. In the next section, however, we focus on CCS and HC_5N emission in the B1 region, and

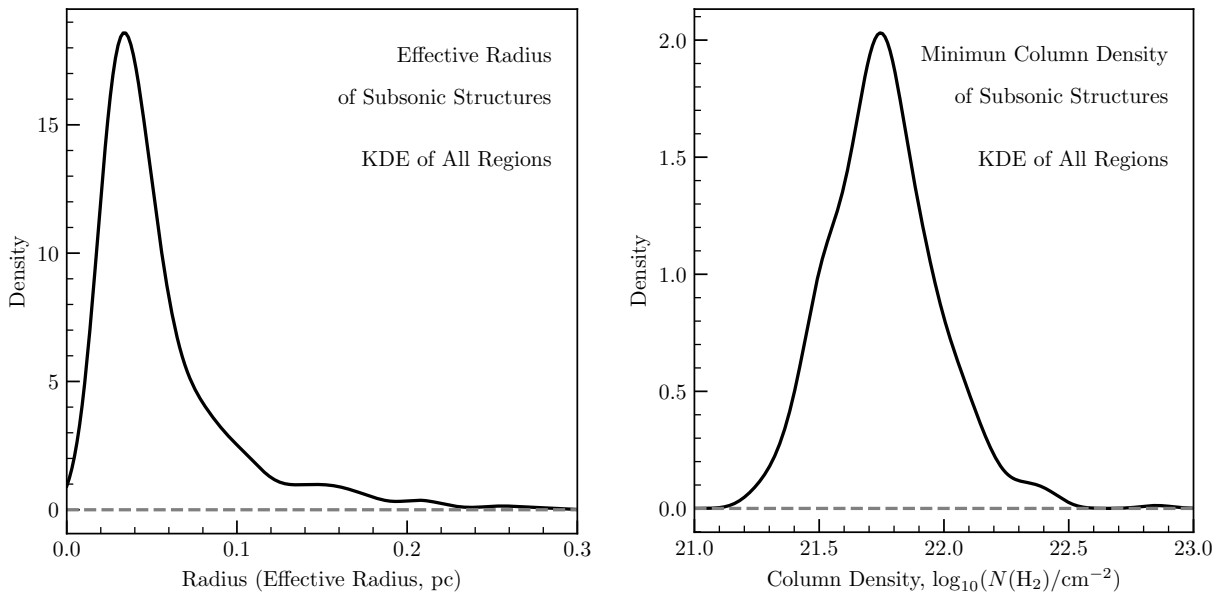


Figure 5. KDE of the effective radius and minimum column density of subsonic structures across all regions. In both cases, the distributions exhibit peaks (representative values) but span a wide range, indicating the absence of a universal value for these structures. Left: distribution of the effective radius ($R_{\text{eff}} = \sqrt{A/\pi}$) for all subsonic structures, which shows a peak at ≈ 0.05 pc, with a pronounced tail extending up to 0.3 pc. Right: distribution of the minimum H_2 column density within subsonic structures, which shows a peak near $6 \times 10^{21} \text{ cm}^{-2}$ and covers a broad range, spanning more than an order of magnitude.

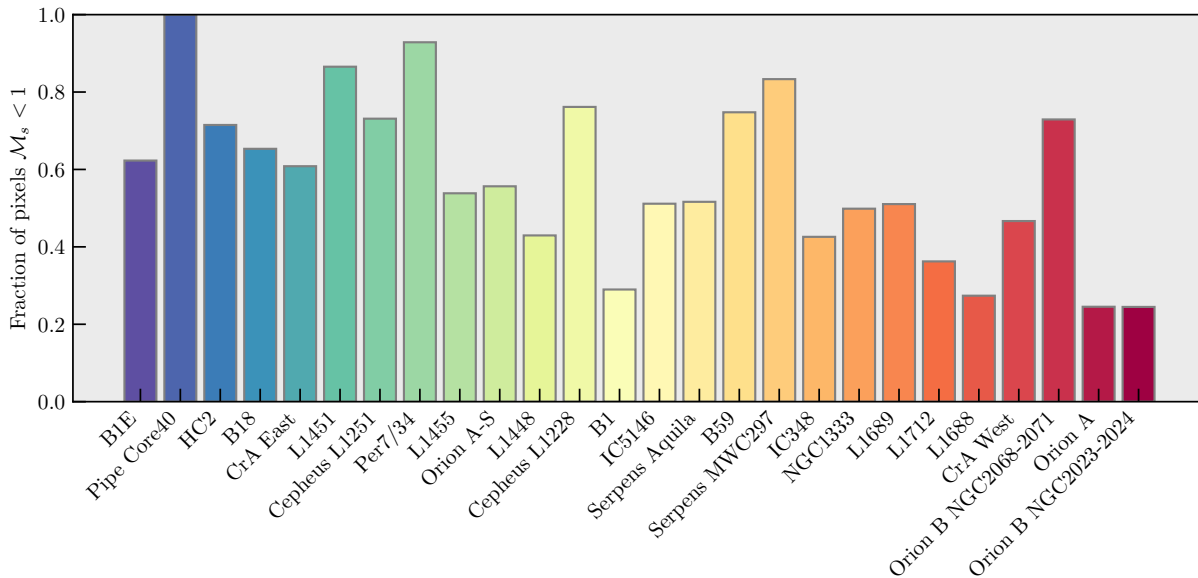


Figure 6. Fraction of subsonic nonthermal velocity dispersion present in the different regions. In the case of B1E and Pipe Core 40, we assume a temperature of 10 K. They are ordered and sorted by increasing mean T_K , as in Figure 3.

show how the carbon-chain molecular emission extends a previously detected infalling streamer of gas from small (disk) scales to clump scales.

4.4. Origin of Streamers: Kinematical Connection

Recently, interferometric observations of young stellar objects revealed the presence of asymmetric infall along linear “streamers.” These structures deliver mass from beyond the dense core down to the disk (or disk scales, see A. Garufi et al. 2022; J. E. Pineda et al. 2020; T. J. Thieme et al. 2022; M. T. Valdivia-Mena et al. 2022, 2023; C. Flores et al. 2023; T. H. Hsieh et al. 2023; J. Speedie et al. 2025). Unfortunately, most observations detect these streamers only up to the angular extents of the interferometers’ primary beams.

Our large-area maps reveal a new region in Perseus with emission from C_2S and HC_5N that extends beyond a previously observed streamer. We show in Figure 7(a) the large-area NH_3 (1,1) map of the Barnard 1 region, which includes the core hosting the young stellar object (YSO), Per-emb-2. We zoom into the Per-emb-2 YSO in the NH_3 and HC_5N emission in Figures 7(b) and (c), respectively. These figures show that NH_3 is related to the dense core, while the HC_5N traces a different structure, an extension to a previously seen streamer shown in the contours. This spatial connection suggests that the streamer is linked to the larger gas reservoir seen in our data, see also K. Taniguchi et al. (2024) for a more detailed abundance determination.

Table 4
Regions with HC₅N Detections

Region	$\log N(\text{HC}_5\text{N})$	$\log N(\text{NH}_3)$	$\log X(\text{HC}_5\text{N}/\text{NH}_3)$	$\log N(\text{H}_2)$	$\log X(\text{HC}_5\text{N}/\text{H}_2)$
B1	12.44 ^{0.27} _{-0.20}	14.25 ^{0.35} _{-0.30}	-1.81 ^{0.40} _{-0.33}	21.05 ^{0.47} _{-0.33}	-9.63 ^{0.35} _{-0.39}
B18	12.65 ^{0.40} _{-0.28}	14.02 ^{0.28} _{-0.22}	-1.33 ^{0.43} _{-0.33}	21.18 ^{0.29} _{-0.21}	-9.38 ^{0.36} _{-0.39}
Cepheus L1228	12.59 ^{0.31} _{-0.23}	14.01 ^{0.40} _{-0.17}	-1.51 ^{0.51} _{-0.37}	20.99 ^{0.30} _{-0.27}	-9.35 ^{0.36} _{-0.26}
Cepheus L1251	12.53 ^{0.26} _{-0.20}	14.19 ^{0.23} _{-0.27}	-1.63 ^{0.33} _{-0.40}	20.98 ^{0.36} _{-0.17}	-9.54 ^{0.23} _{-0.28}
CrAeast	12.92 ^{0.27} _{-0.22}	14.34 ^{0.12} _{-0.16}	-1.39 ^{0.41} _{-0.30}	21.39 ^{0.36} _{-0.22}	-9.26 ^{0.26} _{-0.39}
HC2	12.72 ^{0.49} _{-0.32}	13.94 ^{0.29} _{-0.18}	-1.09 ^{0.60} _{-0.36}	21.49 ^{0.21} _{-0.24}	-9.31 ^{0.43} _{-0.31}
IC 5146	12.68 ^{0.02} _{-0.11}	14.26 ^{0.02} _{-0.04}	-1.60 ^{0.03} _{-0.03}	21.19 ^{0.39} _{-0.28}	-9.59 ^{0.01} _{-0.11}
L1448	12.63 ^{0.18} _{-0.21}	14.37 ^{0.23} _{-0.19}	-1.72 ^{0.18} _{-0.29}	20.96 ^{0.38} _{-0.23}	-9.61 ^{0.22} _{-0.37}
L1451	12.50 ^{0.35} _{-0.15}	14.13 ^{0.09} _{-0.19}	-1.30 ^{0.20} _{-0.19}	21.02 ^{0.40} _{-0.21}	-9.26 ^{0.27} _{-0.18}
NGC 1333	12.34 ^{0.26} _{-0.25}	14.18 ^{0.10} _{-0.19}	-1.85 ^{0.31} _{-0.21}	21.07 ^{0.39} _{-0.22}	-9.68 ^{0.21} _{-0.22}
OrionA	12.60 ^{0.23} _{-0.22}	14.38 ^{0.25} _{-0.30}	-1.73 ^{0.32} _{-0.24}	21.24 ^{0.49} _{-0.41}	-9.69 ^{0.33} _{-0.26}
OrionA S	12.73 ^{0.30} _{-0.21}	14.22 ^{0.20} _{-0.27}	-1.42 ^{0.29} _{-0.29}	21.34 ^{0.49} _{-0.35}	-9.48 ^{0.23} _{-0.26}
Serpens Aquila	12.72 ^{0.23} _{-0.19}	14.23 ^{0.32} _{-0.23}	-1.56 ^{0.34} _{-0.22}	21.56 ^{0.21} _{-0.17}	-9.26 ^{0.24} _{-0.20}

Note. Values given are the 50th percentile, along with the 16th and 84th percentiles of the parameter distributions for all columns. Column densities and abundances of HC₅N relative to H₂ are calculated over all pixels with good line fits, while the NH₃ column densities and HC₅N abundances relative to NH₃ are calculated in regions where both lines are detected.

We derive the velocity maps for C₂S and HC₅N data from GAS with Gaussian fits and compare them to the extent of the NOEMA-identified streamer in Figure 8. The emission from C₂S and HC₅N displays similar velocity maps, with clear blue velocities at large distances (>10,000 au) and a redder velocity component close to the Per-emb-2 source. The velocity gradient is smooth, suggesting that this extended emission detected in the GAS data traces the likely origin of the streamer.

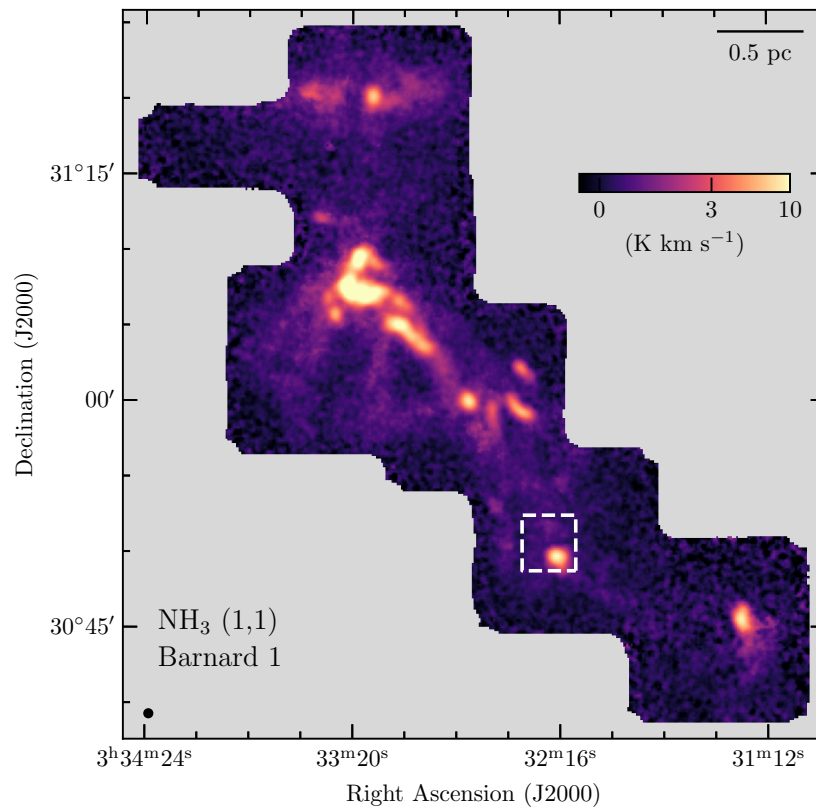
We calculate the velocity difference between HC₅N and NH₃, $\delta v_{\text{LSR}} = v_{\text{LSR}}(\text{HC}_5\text{N}) - v_{\text{LSR}}(\text{NH}_3)$, obtained from the respective line fits and where there is no evidence for multiple velocity components along the line of sight. The difference map and its KDE are shown in Figure 9. The velocity difference map shows that the HC₅N is systematically redshifted with respect to NH₃ by 0.08 km s⁻¹. Similar velocity differences were also reported in Serpens-South (R. K. Friesen et al. 2013) between HC₇N and NH₃. These velocity differences suggest that these molecules are not only tracing different volumes but they also trace infalling motions of more chemically fresh material (J. E. Pineda et al. 2020; M. T. Valdivia-Mena et al. 2024).

Another possibility to explain the velocity difference is the presence of infalling or expanding motions, which are previously seen in different optically thick lines (G. Anglada et al. 1987; D. Mardones et al. 1997; C. W. Lee et al. 1999, 2004; R. K. Friesen et al. 2013). We inspected the emission of HC₅N in the regions shown in Figure 9, and we find that the line profiles are well fitted with a single Gaussian profile without evidence for an asymmetry in them. We also compared the typical difference in the observed velocity dispersion difference (0.02 km s⁻¹) and the non-thermal velocity dispersion (0.008 km s⁻¹), and find that they are comparable or smaller than the typical uncertainty in the observed velocity dispersion (0.02–0.03 km s⁻¹). Therefore, these observations do not support the opacity effect in an expanding or contracting cloud to explain the observations.

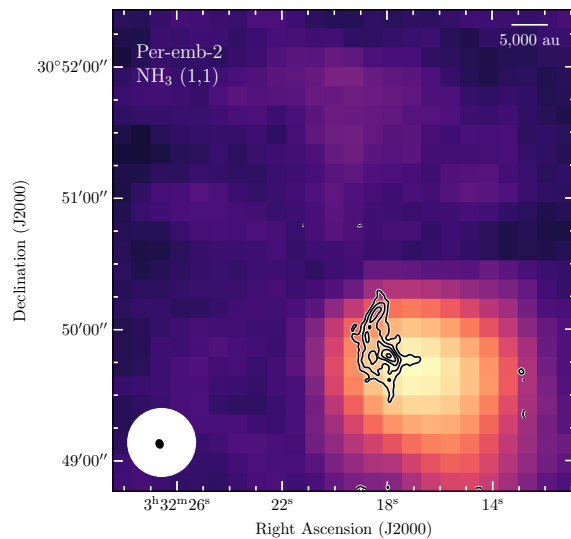
5. Summary

Here, we present the final data release, DR2, from the GAS, where we have mapped a large sample of Northern Hemisphere star-forming clouds in emission from NH₃ (1,1), (2,2), and (3,3), along with HC₅N, HC₇N, and C₂S. We have described the observations, calibration, and combination of the datasets, as well as the line fitting of all observed species. The cubes, moment maps, and maps of the fitted parameters are publicly available.

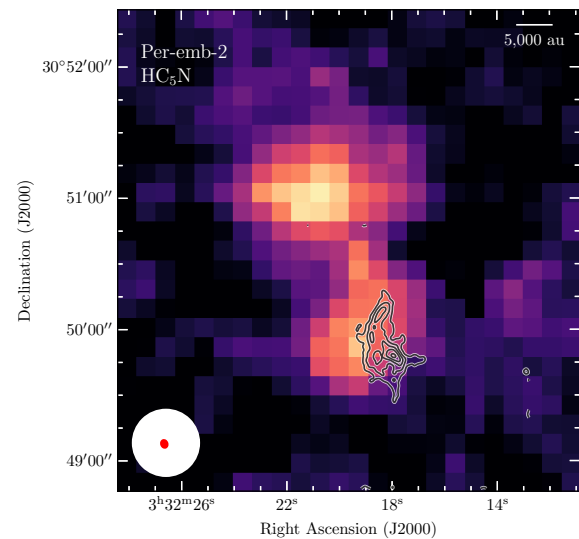
1. We use the NH₃ single velocity component fit to determine the physical properties of the dense gas in the regions covered. The kinetic temperature, T_{K} , appears correlated with the mean value of the σ_v in the region, as well as the maximum value of σ_v . This trend points to the widespread role of feedback from recent star formation on larger scales.
2. We combine the kinetic temperature and velocity dispersion determinations to estimate the nonthermal velocity dispersion across the regions. We find that regions with subsonic levels of nonthermal velocity dispersion are commonly present across different star-forming regions. We find that the fraction of pixels with subsonic levels correlates well with the median kinetic temperature in the region. Even in active regions, such as Orion A or Orion B, approximately 20% of the pixels display subsonic levels of nonthermal velocity dispersion.
3. We do not find a typical or universal column density at which the nonthermal velocity dispersion is mostly subsonic.
4. We find that the $\log_{10} X(\text{NH}_3)$ in individual regions varies between -7.7 and -8.2 , with a typical value of -8.0 when taking all clouds into account. We do not detect evidence for NH₃ depletion, likely due to the angular resolution of the GAS observations.



(a)



(b)



(c)

Figure 7. Extension of the streamer in HC_5N beyond the NH_3 core. Panel (a) shows the large-area NH_3 (1,1) map of the Barnard 1 region, which includes Per-emb-2. The dashed box marks the zoom-in region around Per-emb-2. Panels (b) and (c) show the zoom-in of the NH_3 (1,1) and HC_5N emission, respectively, overlaid with the HC_3N (10–9) integrated intensity from NOEMA (J. E. Pineda et al. 2020). The beam sizes and scale bars are shown in the bottom left and top right corners, respectively.

5. The typical abundance ratio between HC_5N and NH_3 ranges from -1.8 and -1.0 dex.
6. We generate a core catalog of structures identified in NH_3 using a dendrograms analysis and which are matched with continuum catalogs.

7. We explore the possibility of finding the origin of streamers by focusing on Per-emb-2 and comparing the relative HC_5N and NH_3 centroid velocities. We find that HC_5N is systematically redshifted with respect to NH_3 in this source.

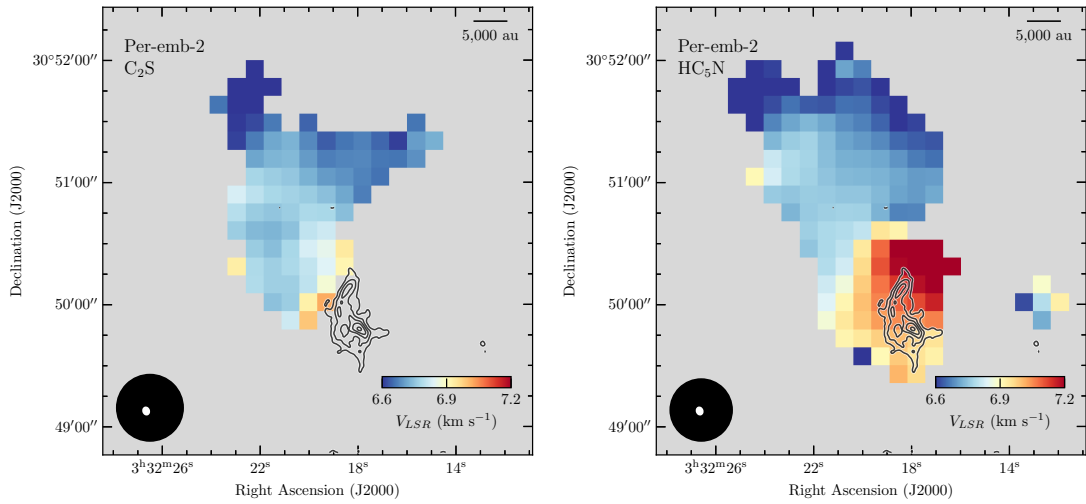


Figure 8. Velocity maps obtained toward Per-emb-2 from a single Gaussian fit to the C₂S and HC₅N data cubes from GAS. A clear velocity gradient connects the streamer and the main gas reservoir. Overlaid in contours is the HC₃N (10–9) integrated intensity from NOEMA (J. E. Pineda et al. 2020). The beam sizes and scale bars are shown in the bottom left and top right corners, respectively.

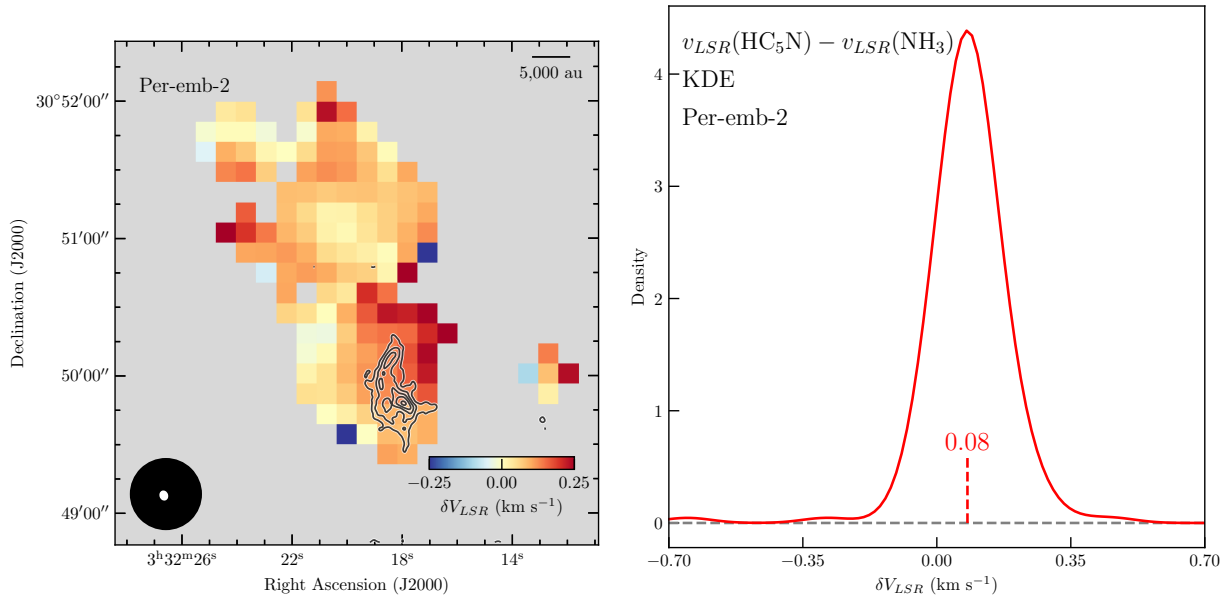


Figure 9. Velocity differences between HC₅N and NH₃ line emission. Left panel shows the velocity difference between a single Gaussian fit to the HC₅N line and the hyperfine fit of NH₃ obtained by GAS. A clear velocity gradient connects the streamer and the main gas reservoir. Overlaid in contours is the HC₃N (10–9) integrated intensity from NOEMA (J. E. Pineda et al. 2020). The beam sizes and scale bars are shown in the bottom left and top right corners, respectively. The right panel shows the KDE of the velocity difference in the regions shown in the left panel. The vertical line shows the median value of the velocity difference.

Acknowledgments

The authors thank the Green Bank Observatory staff who supported this project. The Green Bank Observatory is a facility of the National Science Foundation operated under cooperative agreement by Associated Universities, Inc. Part of this work was supported by the Max-Planck Society. Y.S. was partially supported by an Astronomy and Astrophysics grant AST-2205474 from the National Science Foundation. H.K. acknowledges support from an NSERC Discovery Grant. A.G. acknowledges support from the NSF under grant CAREER 2142300. S.O. acknowledges support from a Peter O’Donnell Distinguished Researcher Fellowship and a Donald Harrington Fellowship. This research used the Canadian Advanced Network For Astronomy Research (CANFAR; S. Gaudet et al. 2010) operated in partnership by the Canadian Astronomy Data Centre and The Digital Research Alliance

of Canada with support from the National Research Council of Canada the Canadian Space Agency, CANARIE and the Canadian Foundation for Innovation.

Facility: GBT.

Software: Astropy (Astropy Collaboration et al. 2013, 2018), pyspeckit (A. Ginsburg & J. Mirocha 2011; A. Ginsburg et al. 2022), matplotlib (J. D. Hunter 2007), spicky (P. Virtanen et al. 2020).

Appendix A Map Noise Levels

We show in Figure 10 histograms of the rms noise per pixel toward each GAS region for each spectral window. The complete figure set (26 figures) is available online. This figure shows that the rms values are not Gaussian, with the majority of pixels having rms values around one value, but with a significant

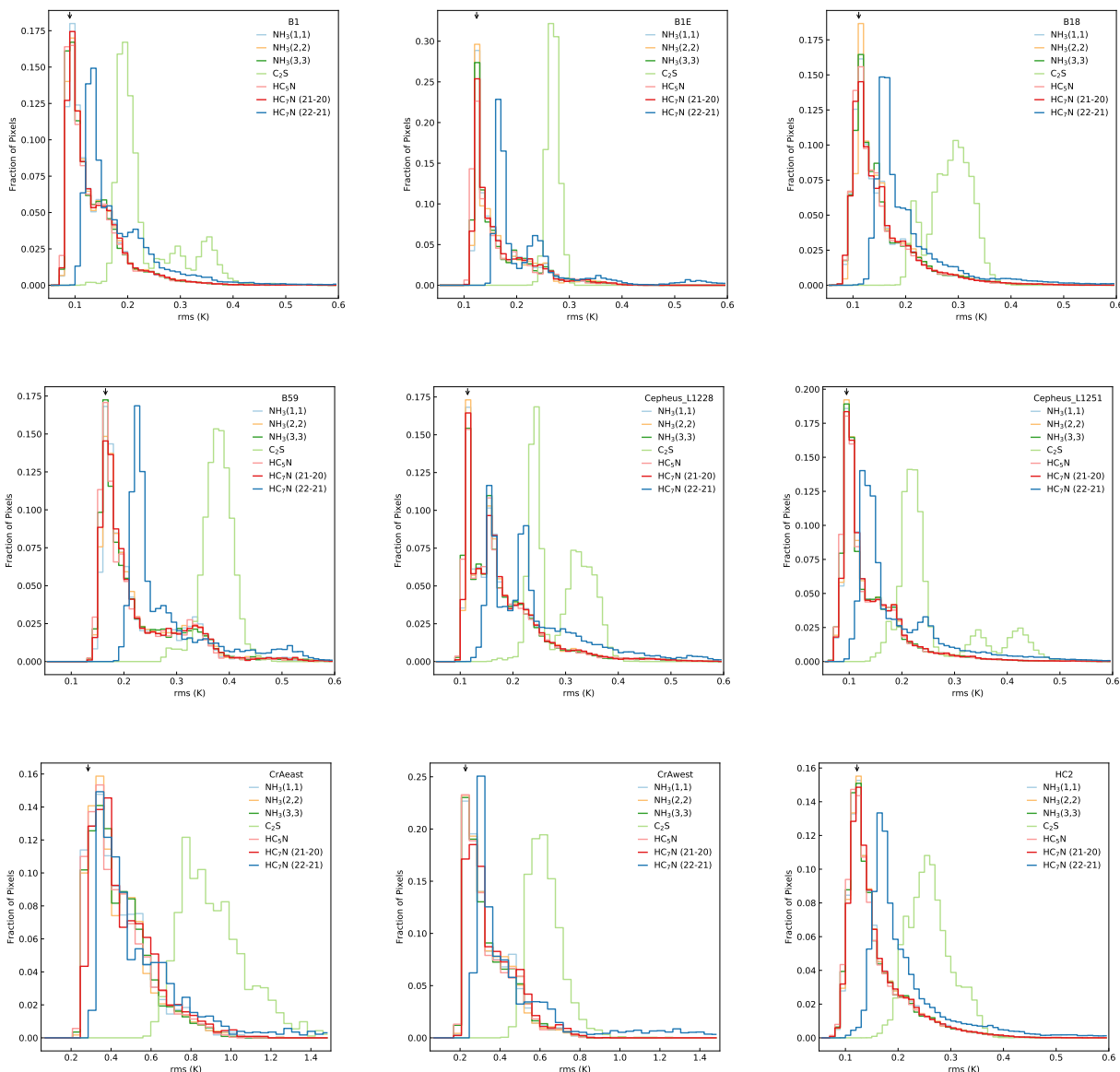


Figure 10. Histograms of noise values per pixel toward each of the GAS regions for all observed lines. The black arrow shows the mode of the rms values for the NH_3 (1,1) spectral window. The complete collection of histograms is available online.

(The complete figure set (26 images) is available in the [online article](#).)

tail to greater rms. As mentioned earlier, this behavior is largely due to the nonuniform coverage of the maps from scanning with the hexagonal arrangement of seven beams with beam centers separated by $\approx 95''$ in the KFPA, but also results from varying weather conditions in the different map blocks. To best describe the noise properties of the majority of the data, we list in Table 5 the mode (rather than the mean or median) and median absolute

deviation (MAD, rather than the standard deviation) of the rms distribution for each region, for each line observed. To calculate the mode, we round the rms values to three decimal places. For most regions, the mode of the rms lies at roughly ~ 0.1 K for the NH_3 , HC_5N , and HC_7N 21–20 lines, with larger values for C_2S and HC_7N 22–21 as noted above. In general, median rms values tend to be larger than the mode by $\sim 10\%$ – 20% .

Table 5
Noise Properties of Line Maps by Region

Region	NH ₃ (1,1)		NH ₃ (2,2)		NH ₃ (3,3)		C ₂ S ₂₁₋₁₀		HC ₅ N 9-8		HC ₇ N 21-20		HC ₇ N 22-21	
	mode	mad	mode	mad	mode	mad	mode	mad	mode	mad	mode	mad	mode	mad
B1	0.09	0.04	0.09	0.04	0.09	0.04	0.19	0.03	0.09	0.04	0.09	0.04	0.13	0.05
B1E	0.12	0.03	0.12	0.03	0.12	0.03	0.27	0.01	0.12	0.03	0.12	0.03	0.17	0.04
B18	0.11	0.04	0.11	0.04	0.11	0.04	0.30	0.04	0.11	0.04	0.11	0.04	0.16	0.04
B59	0.17	0.04	0.17	0.04	0.17	0.04	0.38	0.03	0.16	0.04	0.17	0.04	0.23	0.05
Cepheus L1228	0.11	0.06	0.12	0.06	0.11	0.06	0.24	0.07	0.11	0.06	0.12	0.06	0.16	0.09
Cepheus L1251	0.10	0.04	0.09	0.04	0.09	0.03	0.22	0.03	0.09	0.04	0.10	0.04	0.13	0.05
CrAeast	0.28	0.14	0.34	0.13	0.40	0.13	0.78	0.16	0.33	0.13	0.39	0.14	0.36	0.19
CrAwest	0.23	0.10	0.22	0.10	0.23	0.10	0.61	0.08	0.23	0.10	0.24	0.11	0.30	0.14
HC2	0.12	0.04	0.12	0.03	0.12	0.03	0.26	0.04	0.12	0.03	0.12	0.04	0.17	0.04
IC 348	0.10	0.03	0.09	0.03	0.09	0.03	0.21	0.03	0.09	0.03	0.10	0.03	0.13	0.03
IC 5146	0.10	0.07	0.11	0.07	0.10	0.07	0.31	0.07	0.10	0.07	0.10	0.07	0.14	0.12
L1448	0.12	0.02	0.12	0.02	0.11	0.02	0.27	0.02	0.11	0.02	0.12	0.02	0.16	0.03
L1451	0.12	0.03	0.11	0.03	0.12	0.03	0.25	0.02	0.11	0.03	0.11	0.03	0.15	0.03
L1455	0.10	0.02	0.10	0.02	0.10	0.02	0.23	0.03	0.10	0.02	0.10	0.02	0.15	0.04
L1688	0.12	0.03	0.12	0.03	0.12	0.03	0.32	0.06	0.11	0.03	0.11	0.03	0.16	0.05
L1689	0.13	0.04	0.13	0.04	0.13	0.04	0.30	0.03	0.13	0.04	0.14	0.04	0.18	0.04
L1712	0.14	0.05	0.14	0.05	0.14	0.04	0.32	0.02	0.14	0.04	0.14	0.04	0.19	0.05
NGC 1333	0.11	0.01	0.11	0.01	0.10	0.02	0.27	0.02	0.11	0.01	0.10	0.01	0.15	0.03
OrionA	0.10	0.03	0.10	0.03	0.10	0.03	0.23	0.05	0.11	0.03	0.10	0.03	0.15	0.05
OrionA S	0.15	0.06	0.15	0.06	0.15	0.06	0.35	0.05	0.14	0.06	0.16	0.07	0.20	0.07
OrionB NGC 2023-2024	0.09	0.03	0.10	0.03	0.09	0.03	0.20	0.04	0.09	0.03	0.10	0.03	0.13	0.04
OrionB NGC 2068-2071	0.19	0.07	0.19	0.07	0.19	0.07	0.41	0.12	0.19	0.07	0.20	0.07	0.26	0.10
Perseus	0.18	0.07	0.17	0.07	0.17	0.07	0.45	0.06	0.17	0.07	0.18	0.07	0.24	0.07
Pipe Core 40	0.18	0.07	0.18	0.07	0.18	0.07	0.42	0.02	0.17	0.07	0.18	0.07	0.24	0.08
Serpens Aquila	0.13	0.03	0.13	0.03	0.13	0.03	0.29	0.05	0.13	0.03	0.27	0.11	0.16	0.03
Serpens MWC 297	0.18	0.06	0.18	0.06	0.18	0.06	0.46	0.05	0.19	0.06	0.20	0.07	0.24	0.07

Appendix B

Column Densities and Abundances of C₂S and HC₇N

Here, we provide similar measurements of the column densities of C₂S and HC₇N, and their abundances with respect to NH₃ and H₂, as in Tables 6 and 7, respectively. For C₂S, we

list the median and (16th, 84th) values for each parameter, while we only provide the mean values for HC₇N due to its limited distribution. The column densities and abundances of HC₇N were calculated based on the $J = 21-20$ rotational transition only.

Table 6
Regions with C₂S Detections

Region	log $N(\text{C}_2\text{S})$	log $N(\text{NH}_3)$	log $X(\text{C}_2\text{S}/\text{NH}_3)$	log $N(\text{H}_2)$	log $X(\text{C}_2\text{S}/\text{H}_2)$
B1	13.00 ^{0.16} _{-0.18}	14.13 ^{0.26} _{-0.28}	-1.11 ^{0.25} _{-0.24}	21.05 ^{0.47} _{-0.33}	-9.11 ^{0.28} _{-0.24}
B18	13.14 ^{0.24} _{-0.16}	14.00 ^{0.23} _{-0.20}	-0.78 ^{0.34} _{-0.33}	21.18 ^{0.29} _{-0.21}	-8.87 ^{0.28} _{-0.26}
HC2	13.26 ^{0.28} _{-0.25}	13.95 ^{0.30} _{-0.18}	-0.57 ^{0.36} _{-0.41}	21.49 ^{0.21} _{-0.24}	-8.76 ^{0.26} _{-0.24}
Serpens Aquila	13.32 ^{0.19} _{-0.19}	14.06 ^{0.30} _{-0.15}	-0.79 ^{0.27} _{-0.41}	21.56 ^{0.21} _{-0.17}	-8.59 ^{0.20} _{-0.21}

Note. Values given are the 50th percentile, along with the 16th and 84th percentiles of the parameter distributions for all columns. Column densities and abundances of C₂S relative to H₂ are calculated over all pixels with good line fits, while the NH₃ column densities and C₂S abundances relative to NH₃ are calculated in regions where both lines are detected.

Table 7
Regions with HC₇N Detections

Region	$\log N(\text{HC}_7\text{N})$	$\log N(\text{NH}_3)$	$\log X(\text{HC}_7\text{N}/\text{NH}_3)$	$\log N(\text{H}_2)$	$\log X(\text{HC}_7\text{N}/\text{H}_2)$
B1	13.31	20.84	-7.54
HC2	12.89	13.97	-1.05	22.11	-9.23

Note. Values given are the mean values of the parameter distributions for all columns. Column densities and abundances of HC₇N relative to H₂ are calculated over all pixels with good line fits, based on the HC₇N_J = 21–20 emission line. The NH₃ column densities and HC₇N abundances relative to NH₃ are calculated in regions where both lines are detected. We do not detect HC₇N in sufficiently large areas to provide percentiles.

Appendix C Core Catalog

The core catalog is provided in Table 8, with the full version available online. This table includes the region, the index number, the R.A. and decl. coordinates, the core radius and mass, and the protostellar content as reported in

A. Pandhi et al. (2023). In addition we derived the mean LSR velocity, the mean observed velocity dispersion, the excitation and kinetic temperature, the NH₃ column density, the thermal and nonthermal velocity dispersions, the matched continuum ID, and the estimated virial parameters (see Equations (5) and (6)).

Table 8
NH₃ Core Properties for Selected Regions

Region	GAS ^a	R.A. (J2000)	Decl. (J2000)	v_{LSR} (km s ⁻¹)	σ_v (km s ⁻¹)	T_{ex} (K)	T_{K} (K)	$\log N(\text{NH}_3)$ (cm ⁻²)	σ_{th} (km s ⁻¹)	σ_{NT} (km s ⁻¹)	Continuum ID	R (pc)	M (M_{\odot})	α_{vir}	Type
B1	3	3:32:16.5	30:49:32.0	6.80 (0.11)	0.21 (0.05)	4.75 (1.01)	11.05 (0.82)	14.1 (0.2)	0.20	0.20	033217.8+304948	0.01	1.5	0.6	protostellar
B1	5	3:32:19.5	30:51:36.0	6.56 (0.07)	0.20 (0.07)	3.60 (0.30)	11.30 (0.00)	13.9 (0.0)	0.20	0.19	033218.9+305148	0.03	0.1	17.4	prestellar
B1	4	3:32:32.6	30:50:26.9	6.57 (0.08)	0.24 (0.16)	3.70 (0.51)	10.71 (0.54)	13.9 (0.1)	0.19	0.22	033232.0+305030	0.03	0.9	3.9	prestellar
B1	11	3:32:34.0	30:56:29.4	6.54 (0.05)	0.38 (0.08)	3.19 (0.13)	11.82 (0.00)	14.2 (0.1)	0.20	0.38	033233.3+305627	0.04	0.2	44.3	prestellar
B1	6	3:32:35.6	30:52:56.9	6.84 (0.13)	0.17 (0.10)	3.94 (0.70)	9.99 (1.32)	13.7 (0.1)	0.19	0.15	033236.7+305306	0.04	0.4	10.0	prestellar
B1	27	3:32:44.3	30:59:59.1	6.72 (0.11)	0.20 (0.07)	4.99 (0.81)	10.26 (0.73)	14.1 (0.2)	0.19	0.18	033243.7+305948	0.05	3.1	1.5	prestellar
B1	58	3:33:01.9	31:20:53.3	6.64 (0.03)	0.28 (0.04)	4.07 (0.60)	10.84 (2.20)	14.0 (0.1)	0.19	0.27	033300.8+312047	0.05	1.4	4.4	prestellar
B1	34	3:33:03.1	31:04:33.0	6.62 (0.05)	0.16 (0.03)	5.95 (0.52)	9.92 (0.46)	14.2 (0.2)	0.19	0.15	033302.5+310432	0.02	0.8	1.8	prestellar
B1	40	3:33:05.4	31:06:30.5	6.57 (0.02)	0.16 (0.01)	5.59 (0.24)	10.09 (0.35)	14.2 (0.1)	0.19	0.14	033305.0+310640	0.02	1.6	0.9	prestellar
B1	43	3:33:16.5	31:06:59.5	6.33 (0.08)	0.25 (0.01)	7.78 (0.31)	11.42 (0.20)	14.7 (0.0)	0.20	0.24	033316.4+310652	0.01	0.8	1.4	protostellar
B1	45	3:33:18.0	31:09:19.8	6.32 (0.19)	0.31 (0.04)	7.00 (0.59)	11.78 (0.72)	14.5 (0.1)	0.20	0.30	033317.7+310932	0.01	2.7	0.6	protostellar

Notes. NH₃ core catalog crossmatched with submillimeter continuum core catalogs, first presented by A. Pandhi et al. (2023). Here, we provide mean and standard deviation values for NH₃ fit parameters within the NH₃ core contours as determined from the dendrogram analysis. Continuum core parameters, and core type, are taken from the continuum catalogs cited in A. Pandhi et al. (2023), or determined directly therein.

^a GAS ID from dendrogram analysis as listed in A. Pandhi et al. (2023). Note that GAS core IDs are unique only within regions.

(This table is available in its entirety in machine-readable form in the [online article](#).)

Appendix D

Comparison Temperature and Velocity Dispersion

Figure 3 shows a correlation between the velocity dispersion, σ_v , and the gas kinetic temperature, T_K , across different regions using violin plots. Figure 11 further demonstrates that the typical velocity dispersion in the different regions cannot be explained solely by an increase in T_K . The data span from subsonic levels of nonthermal velocity dispersion to supersonic values, reaching up to $\mathcal{M}_s = 2$. This is similar to the strong correlation found by R. K. Friesen & E. Jarvis (2024) in Serpens-South.

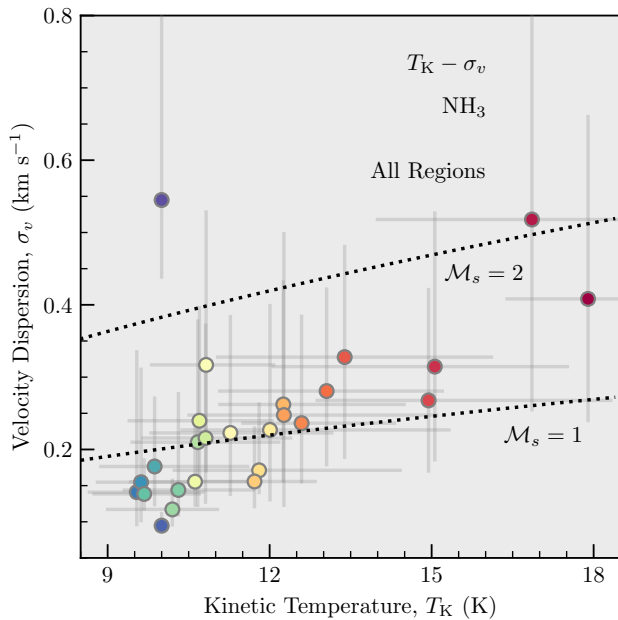


Figure 11. Comparison of typical velocity dispersion and kinetic temperature for all regions. Symbols show the 50th, 16th, and 84th percentiles of the values for each region, with asymmetric uncertainties. The color of the symbols corresponds to the mean T_K , consistent with Figure 3. The dotted lines indicate the expected velocity dispersions for sonic Mach numbers of $\mathcal{M}_s = 1$ and $\mathcal{M}_s = 2$.

ORCID iDs

Jaime E. Pineda <https://orcid.org/0000-0002-3972-1978>
 Rachel K. Friesen <https://orcid.org/0000-0001-7594-8128>
 Erik Rosolowsky <https://orcid.org/0000-0002-5204-2259>
 Ana Chacón-Tanarro <https://orcid.org/0000-0001-8804-8604>
 Michael Chun-Yuan Chen <https://orcid.org/0000-0003-4242-973X>
 James Di Francesco <https://orcid.org/0000-0002-9289-2450>
 Helen Kirk <https://orcid.org/0000-0002-5779-8549>
 Anna Punanova <https://orcid.org/0000-0001-6004-875X>
 Youngmin Seo <https://orcid.org/0000-0003-2122-2617>
 Yancy Shirley <https://orcid.org/0000-0002-0133-8973>
 Adam Ginsburg <https://orcid.org/0000-0001-6431-9633>
 Stella S. R. Offner <https://orcid.org/0000-0003-1252-9916>
 Ayush Pandhi <https://orcid.org/0000-0002-8897-1973>
 Ayushi Singh <https://orcid.org/0000-0001-6022-3618>
 Feiyu Quan <https://orcid.org/0009-0006-9160-1021>
 Héctor G. Arce <https://orcid.org/0000-0001-5653-7817>

Paola Caselli <https://orcid.org/0000-0003-1481-7911>
 Spandan Choudhury <https://orcid.org/0000-0002-7497-2713>
 Alyssa A. Goodman <https://orcid.org/0000-0003-1312-0477>
 Fabian Heitsch <https://orcid.org/0000-0002-4775-039X>
 Peter G. Martin <https://orcid.org/0000-0002-5236-3896>
 Christopher D. Matzner <https://orcid.org/0000-0001-9732-2281>
 Philip C. Myers <https://orcid.org/0000-0002-2885-1806>
 Elena Redaelli <https://orcid.org/0000-0002-0528-8125>
 Samantha Scibelli <https://orcid.org/0000-0002-9485-4394>

References

- Abergel, A., Bernard, J. P., Boulanger, F., et al. 1996, *A&A*, **315**, L329
 Aikawa, Y., Ohashi, N., Inutsuka, S.-i., Herbst, E., & Takakuwa, S. 2001, *ApJ*, **552**, 639
 Alexander, A. J., Kroto, H. W., & Walton, D. R. M. 1976, *JMoSp*, **62**, 175
 André, P., Men'shchikov, A., Bontemps, S., et al. 2010, *A&A*, **518**, L102
 Anglada, G., Rodríguez, L. F., Canto, J., Estalella, R., & López, R. 1987, *A&A*, **186**, 280
 Astropy Collaboration, Price-Whelan, A. M., Sipőcz, B. M., et al. 2018, *AJ*, **156**, 123
 Astropy Collaboration, Robitaille, T. P., Tollerud, E. J., et al. 2013, *A&A*, **558**, A33
 Bachiller, R., & Cernicharo, J. 1986, *A&A*, **168**, 262
 Benson, P. J., & Myers, P. C. 1983, *ApJ*, **270**, 589
 Benson, P. J., & Myers, P. C. 1989, *ApJS*, **71**, 89
 Bertoldi, F., & McKee, C. F. 1992, *ApJ*, **395**, 140
 Caselli, P., Pineda, J. E., Sipilä, O., et al. 2022, *ApJ*, **929**, 13
 Caselli, P., Walmsley, C. M., Tafalla, M., Dore, L., & Myers, P. C. 1999, *ApJL*, **523**, L165
 Chen, C.-Y., Behrens, E. A., Washington, J. E., et al. 2020, *MNRAS*, **494**, 1971
 Chen, H. H.-H., Pineda, J. E., Goodman, A. A., et al. 2019, *ApJ*, **877**, 93
 Chen, M. C.-Y., Di Francesco, J., Rosolowsky, E., et al. 2020, *ApJ*, **891**, 84
 Chen, X., Launhardt, R., & Henning, T. 2009, *ApJ*, **691**, 1729
 Chini, R., Reipurth, B., Sievers, A., et al. 1997, *A&A*, **325**, 542
 Choudhury, S., Pineda, J. E., Caselli, P., et al. 2020, *A&A*, **640**, L6
 Choudhury, S., Pineda, J. E., Caselli, P., et al. 2021, *A&A*, **648**, A114
 Codella, C., Welser, R., Henkel, C., Benson, P. J., & Myers, P. C. 1997, *A&A*, **324**, 203
 Crapsi, A., Caselli, P., Walmsley, M. C., & Tafalla, M. 2007, *A&A*, **470**, 221
 Dunham, M. M., Allen, L. E., Evans, N. J. I., et al. 2015, *ApJS*, **220**, 11
 Dzib, S. A., Loinard, L., Ortiz-León, G. N., Rodríguez, L. F., & Galli, P. A. B. 2018, *ApJ*, **867**, 151
 Fehér, O., Tóth, L. V., Ward-Thompson, D., et al. 2016, *A&A*, **590**, A75
 Flores, C., Ohashi, N., Tobin, J. J., et al. 2023, *ApJ*, **958**, 98
 Friesen, R. K., Di Francesco, J., Shirley, Y. L., & Myers, P. C. 2009, *ApJ*, **697**, 1457
 Friesen, R. K., & Jarvis, E. 2024, *ApJ*, **969**, 70
 Friesen, R. K., Medeiros, L., Schnee, S., et al. 2013, *MNRAS*, **436**, 1513
 Friesen, R. K., Pineda, J. E., co-PIs, et al. 2017, *ApJ*, **843**, 63
 Galli, P. A. B., Loinard, L., Ortiz-León, G. N., et al. 2018, *ApJ*, **859**, 33
 Garufi, A., Podio, L., Codella, C., et al. 2022, *A&A*, **658**, A104
 Gaudet, S., Hill, N., Armstrong, P., et al. 2010, *Proc. SPIE*, **7740**, 774011
 Ginsburg, A., & Mirocha, J., 2011 PySpecKit: Python Spectroscopic Toolkit, Astrophysics Source Code Library, ascl:1109.001
 Ginsburg, A., Sokolov, V., de Val-Borro, M., et al. 2022, *AJ*, **163**, 291
 Goodman, A. A., Barranco, J. A., Wilner, D. J., & Heyer, M. H. 1998, *ApJ*, **504**, 223
 Griffin, M. J., Abergel, A., Abreu, A., et al. 2010, *A&A*, **518**, L3
 Großschedl, J. E., Alves, J., Meingast, S., et al. 2018, *A&A*, **619**, A106
 Hacar, A., Tafalla, M., Forbrich, J., et al. 2018, *A&A*, **610**, A77
 Hirota, T., Oishi, M., & Yamamoto, S. 2009, *ApJ*, **699**, 585
 Ho, P. T. P., & Townes, C. H. 1983, *ARA&A*, **21**, 239
 Hsieh, T. H., Segura-Cox, D. M., Pineda, J. E., et al. 2023, *A&A*, **669**, A137
 Hunter, J. D. 2007, *CSE*, **9**, 90
 Jijina, J., Myers, P. C., & Adams, F. C. 1999, *ApJS*, **125**, 161
 Johnstone, D., Di Francesco, J., & Kirk, H. 2004, *ApJL*, **611**, L45
 Kaifu, N., Oishi, M., Kawaguchi, K., et al. 2004, *PASJ*, **56**, 69

- Kauffmann, J., Bertoldi, F., Bourke, T. L., Evans, N. J. I., & Lee, C. W. 2008, *A&A*, **487**, 993
- Keown, J., Di Francesco, J., Kirk, H., et al. 2017, *ApJ*, **850**, 3
- Kerr, R., Kirk, H., Di Francesco, J., et al. 2019, *ApJ*, **874**, 147
- Kirk, H., Friesen, R. K., Pineda, J. E., et al. 2017, *ApJ*, **846**, 144
- Kounkel, M., Covey, K., Suárez, G., et al. 2018, *AJ*, **156**, 84
- Kroto, H. W., Kirby, C., Walton, D. R. M., et al. 1978, *ApJL*, **219**, L133
- Lee, C. W., Myers, P. C., & Plume, R. 2004, *ApJS*, **153**, 523
- Lee, C. W., Myers, P. C., & Tafalla, M. 1999, *ApJ*, **526**, 788
- Lin, Y., Spezzano, S., Pineda, J. E., et al. 2023, *A&A*, **680**, A43
- Little, L. T., MacDonald, G. H., Riley, P. W., & Matheson, D. N. 1979, *MNRAS*, **189**, 539
- Mallick, K. K., Kumar, M. S. N., Ojha, D. K., et al. 2013, *ApJ*, **779**, 113
- Mangum, J. G., & Shirley, Y. L. 2015, *PASP*, **127**, 266
- Mardones, D., Myers, P. C., Tafalla, M., et al. 1997, *ApJ*, **489**, 719
- McDowell, R. S. 1988, *JChPh*, **88**, 356
- Myers, P. C., & Benson, P. J. 1983, *ApJ*, **266**, 309
- Neralwar, K. R., Colombo, D., Offner, S., et al. 2024, *A&A*, **690**, A345
- Offner, S. S. R., Taylor, J., Markey, C., et al. 2022, *MNRAS*, **517**, 885
- Ortiz-León, G. N., Loinard, L., Dzib, S. A., et al. 2018a, *ApJ*, **865**, 73
- Ortiz-León, G. N., Loinard, L., Dzib, S. A., et al. 2018b, *ApJL*, **869**, L33
- Pandhi, A., Friesen, R. K., Fissel, L., et al. 2023, *MNRAS*, **525**, 364
- Pineda, J. E., Arzoumanian, D., Andre, P., et al. 2023, in ASP Conf. Ser. 534, *Protostars and Planets VII*, ed. S. Inutsuka et al. (San Francisco, CA: ASP), 233
- Pineda, J. E., Goodman, A. A., Arce, H. G., et al. 2010, *ApJL*, **712**, L116
- Pineda, J. E., Harju, J., Caselli, P., et al. 2022, *AJ*, **163**, 294
- Pineda, J. E., Schmiedeke, A., Caselli, P., et al. 2021, *ApJ*, **912**, 7
- Pineda, J. E., Segura-Cox, D., Caselli, P., et al. 2020, *NatAs*, **4**, 1158
- Poglitsch, A., Waelkens, C., Geis, N., et al. 2010, *A&A*, **518**, L2
- Purcell, C. R., Longmore, S. N., Walsh, A. J., et al. 2012, *MNRAS*, **426**, 1972
- Redaelli, E., Bizzocchi, L., Caselli, P., et al. 2019, *A&A*, **629**, A15
- Rosolowsky, E. W., Pineda, J. E., Foster, J. B., et al. 2008, *ApJS*, **175**, 509
- Saito, S., Kawaguchi, K., Yamamoto, S., et al. 1987, *ApJL*, **317**, L115
- Seo, Y. M., Shirley, Y. L., Goldsmith, P., et al. 2015, *ApJ*, **805**, 185
- Singh, A., & Martin, P. G. 2022, *ApJ*, **941**, 135
- Singh, A., Matzner, C. D., Friesen, R. K., et al. 2021, *ApJ*, **922**, 87
- Smith, S. E. T., Friesen, R., Marchal, A., et al. 2023, *MNRAS*, **519**, 285
- Speedie, J., Dong, R., Teague, R., et al. 2025, *ApJL*, **981**, L30
- Storm, S., Mundy, L. G., Lee, K. I., et al. 2016, *ApJ*, **830**, 127
- Suzuki, H., Yamamoto, S., Ohishi, M., et al. 1992, *ApJ*, **392**, 551
- Swift, J. J., Welch, W. J., & Di Francesco, J. 2005, *ApJ*, **620**, 823
- Tafalla, M., Myers, P. C., Caselli, P., & Walmsley, C. M. 2004, *A&A*, **416**, 191
- Tafalla, M., Myers, P. C., Caselli, P., Walmsley, C. M., & Comito, C. 2002, *ApJ*, **569**, 815
- Taniguchi, K., Pineda, J. E., Caselli, P., et al. 2024, *ApJ*, **965**, 162
- Thieme, T. J., Lai, S.-P., Lin, S.-J., et al. 2022, *ApJ*, **925**, 32
- Valdivia-Mena, M. T., Pineda, J. E., Caselli, P., et al. 2024, *A&A*, **687**, A71
- Valdivia-Mena, M. T., Pineda, J. E., Segura-Cox, D. M., et al. 2022, *A&A*, **667**, A12
- Valdivia-Mena, M. T., Pineda, J. E., Segura-Cox, D. M., et al. 2023, *A&A*, **677**, A92
- Virtanen, P., Gommers, R., Oliphant, T. E., et al. 2020, *NatMe*, **17**, 261
- Walmsley, C. M., & Ungerechts, H. 1983, *A&A*, **122**, 164
- Westerhout, G. 1958, *BAN*, **14**, 215
- Wienen, M., Wyrowski, F., Schuller, F., et al. 2012, *A&A*, **544**, A146
- Wu, Y., Zhang, Q., Yu, W., et al. 2006, *A&A*, **450**, 607
- Yan, Q.-Z., Zhang, B., Xu, Y., et al. 2019, *A&A*, **624**, A6
- Zucker, C., Schlafly, E. F., Speagle, J. S., et al. 2018, *ApJ*, **869**, 83